Mesozoic crustal evolution of southern Tibet: Constraints from the Early Jurassic igneous rocks in the central Lhasa terrane

Xin Dong[1, 2], Yaoling Niu[2], Zeming Zhang[1], Zuolin Tian[1], Zhenyu He[1]

1. Key Laboratory of Deep-Earth Dynamics of Ministry of Land and Resources, Institute of Geology, Chinese Academy of Geological Sciences, Beijing, 100037, China
2. Department of Earth Sciences, Durham University, Durham, DH1 3LE, UK

Abstract

Phanerozoic growth of continental crust on our planet is one of the important research themes in Earth Science. Here, we present the results of a systematic study of newly found and previously reported Mesozoic igneous rocks, including diorite cumulate, granodiorite cumulate, mafic magmatic enclaves (MME) and host granitoids in the central Lhasa terrane, southern Tibet. These igneous rocks give zircon U-Pb crystallization ages of 199−189 Ma. Based on constituent mineral and bulk-rock compositions, the cumulates are best understood as resulting from amphibole, plagioclase and titanite crystallization from a mafic andesitic magma. The host granitoids also show compositional systematics consistent with amphibole-plagioclase fractional crystallization from andesitic magma. The MMEs share many characteristics with their host granitoids in common, including identical crystallization age, similar mineralogy, mineral chemistry and zircon isotopic

compositions, representing earlier cumulate derived from the same magmatic system as their host rocks. The magma parental to the studied Early Jurassic igneous rocks is best explained as resulting from partial melting of hydrated ocean crust together with varying continental material. The increasing zircon $\varepsilon_{Hf}(t)$ values of multiple plutons in the central Lhasa terrane with time during ~215−170 Ma indicate its gradual depleted process of crustal evolution.

Keywords:

Cumulates; granitoids; assimilation–fractional crystallization; Mesozoic crustal evolution; southern Tibet

1. Introduction

The Earth is the only planet in the solar system with oceans and continents with the continental crust standing above the sea level (e.g., Rudnick, 1995). The significance of the continental crust on which we live is self-evident, yet our knowledge remains limited on its origin and growth (Niu et al., 2013). Arc magmatism is widely accepted to be a fundamental process responsible for post-Archean continental crust growth (e.g., Rudnick and Gao, 2003; Taylor and McLennan, 1985). Therefore, understanding the origin and nature of arc crusts is critical for understanding the formation and evolution of continental crust (e.g., Jagoutz and Kelemen, 2015).

Unlike the oceanic arc (e.g., Kohistan arc in western Himalaya), the Gangdese

arc resulting from the subduction of the Neo-Tethyan seafloor and subsequent India-Asia collision is a prominent continental arc along the southern margin of Asia, and thus has more complex petrological architecture and geochemical composition due to ancient basement assimilation. The most noteworthy feature of this magmatic arc is its predominantly zircon $\varepsilon_{Hf}(t) > 0$ in the southern Lhasa terrane, and mostly zircon $\varepsilon_{Hf}(t) < 0$ in the central Lhasa terrane (e.g., Chu et al., 2006; Hou et al., 2015; Ji et al., 2009; Zhu et al., 2011). Although there have been many advances in the study of the Gangdese arc magmatism, the processes how magmatic arc is actually developed and what may have caused the across-arc zircon-Hf isotope systematics remain unclear. Moreover, the pre-Cenozoic crustal evolution of the Lhasa terrane is also crucial for understanding the India-Asian continental collision and Tibetan uplift during the Cenozoic.

In this paper, we present bulk-rock major and trace element compositions, mineral chemistry, zircon geochronology, bulk-rock Sr-Nd and zircon Hf isotopic data on the igneous rocks, including Bascong Tso cumulate plutons (<100 km^2) and Mamba MME-bearing granitoid batholith (>100 km^2) of ~200 Ma in the central Lhasa terrane in southern Tibet. Our results suggest that the amphibole-dominated assimilation–fractional crystallization (AFC) is the effective process for the generation of these Early Jurassic igneous rocks. This new understanding details a gradual depleted evolution of crust in the central Lhasa terrane during the Mesozoic.

2. Geological background

The Tibetan Plateau, from north to south, comprises the Songpan-Ganzi flysch complex, Qiangtang and Lhasa terranes, and the Himalaya, separated by the Jinsha, Bangong-Nujiang and Indus-Yarlung Zangbo Suture zones, respectively (Fig. 1a) (e.g., Dewey et al., 1988; Yin and Harrison, 2000; Zhu et al., 2013). As a main tectonic component, the Lhasa terrane in southern Tibet is interpreted to have been rifted from the northern margin of Gondwana in the Triassic and drifted northward to collide with the Qiangtang terrane in the Cretaceous (e.g., Zhu et al., 2013). An Andean-type active continental margin has been proposed in the southern part of the terrane prior to its collision with the northward moving Indian continent in the Cenozoic (e.g., Dewey et al., 1988; Mo et al., 2008; Yin and Harrison, 2000; Zhu et al., 2011, 2013). The Lhasa terrane is subdivided into northern, central, and southern subterranes separated by the Shiquanhe-Nam Tso Mélange zone and the Luobadui-Mila Mountain fault, respectively (Fig. 1b) (e.g., Pan et al., 2004; Zhu et al., 2011).

The southern Lhasa subterrane (SLT) is characterized by the existence of juvenile crust with a Precambrian metamorphic basement locally exposed (e.g., Dong et al., 2020; Ji et al., 2009; Mo et al., 2008; Zhu et al., 2011, 2013). This subterrane is dominated by the Cretaceous–Tertiary batholiths and the Paleogene Linzizong volcanic succession, with minor Triassic–Cretaceous volcano-intrusive rocks (Pan et al., 2004; Zhu et al., 2008, 2013). Several Early Paleozoic and Late Devonian granites have been reported in the eastern SLT (Dong et al., 2010, 2014; Ji et al., 2012; Ma et al., 2019). The central Lhasa subterrane (CLT) was once a microcontinent with Precambrian crystalline basement widespread (Dong et al., 2011a; Harris et al., 1988a;

89 Li, 1955; Zhang et al., 2012), covered by Permo–Carboniferous metasedimentary
90 rocks and Upper Jurassic–Lower Cretaceous strata with abundant volcanic-intrusive
91 rocks, as well as minor Ordovician–Devonian, and Triassic strata (Pan et al., 2004;
92 Zhu et al., 2009, 2011, 2013). The Mesozoic plutonic rocks occur as batholiths of
93 varying age (cf. Zhu et al., 2011 and references therein). The volcanic rocks are
94 mostly early Cretaceous in age with minor being Permian. Cambrian–Ordovician
95 volcanic rocks and an angular unconformity have been documented (e.g., Li et al.,
96 2010; Zhu et al., 2012). The Late Permian high-pressure Sumdo eclogite and Late
97 Triassic–Early Jurassic metamorphic rocks in the middle and eastern CLT indicate
98 subduction of the Sumdo Tethyan seafloor (e.g., Cheng et al., 2015; Dong et al.,
99 2011b; Lin et al., 2013; Weller et al., 2015; Yang et al., 2009; Zeng et al., 2009). The
100 northern Lhasa subterrane (NLT) contains juvenile crust and is covered by Middle
101 Triassic-Cretaceous sedimentary rocks with abundant early Cretaceous volcanic rocks
102 and associated granitoids (Pan et al., 2004; Zhu et al., 2011, 2013).

103 The Gangdese arc along the southern Lhasa terrane extends E-W for > 1500 km
104 with varying width (~ 20 to 60 km; e.g., Zhu et al., 2011). Abundant age data indicate
105 that these magmatic arc rocks were emplaced from the Late Triassic to the Late
106 Miocene (e.g., Zhu et al., 2011), occurring as plutons with two main episodes of
107 magmatic activity in the Late Triassic–Early Jurassic (220–170 Ma) and the Early
108 Cretaceous (95–85 Ma) (e.g., Ji et al., 2009; Zhu et al., 2011). Except for those in the
109 CLT, most plutonic rocks in the SLT have depleted zircon Hf and bulk-rock Sr-Nd
110 isotopic compositions, indicative of significant mantle contributions or a juvenile

crust in their petrogenesis (e.g., Mo et al., 2008; Zhu et al., 2011, 2013). The Early Mesozoic Gangdese arc formed in response to the northward subduction of the Neo-Tethyan seafloor to the south (e.g., Chu et al., 2006; Ji et al., 2009; Zhang et al, 2007b) or to the southward subduction of the Bangong–Nujiang Tethyan seafloor to the north (e.g., Sui et al., 2018; Zhu et al., 2011, 2013).

The samples of this study were collected in the Basong Tso and Mamba areas of the CLT (Fig. 1c–d). In the Basong Tso area, the Early Jurassic and Oligocene plutons intrude the Ordovician strata and the Late Triassic−Early Jurassic metamorphic rocks (Figs. 1c and 2a). The latter metamorphic rocks experienced peak medium-pressure amphibolite-facies metamorphism at ca. 204–192 Ma (Lin et al., 2013; Weller et al., 2015). The Early Jurassic Basong Tso plutons (about 6 km^2) include diorite and granodiorite cumulates, with the former intruding the latter (Fig. 2b–d). In the Mamba area, the Late Triassic−Early Jurassic batholith is about 130 km^2 in outcrop located northwest of the Sumdo eclogite (Fig. 1b–d), and intrudes the Ordovician strata (Figs. 1d and 3a) and has been intruded by the Late Cretaceous granitoids (Meng et al., 2014) (Fig. 1d). The Late Triassic−Early Jurassic Mamba batholith includes host granite, granodiorite and quartz monzodiorte (MME). MMEs widely occur as dark blobs of varying shape (ellipsoidal or elongate) and size (centimeters to decimeters) without chilled margins (Fig. 3b–d).

3. Petrography

This study focuses on the diorite and granodiorite cumulates from the Basong

Tso area, and the MMEs and their host granites and granodiorite from the Mamba area. Sample details, including locations, lithology (based on mineral assemblages and modes), zircon U-Pb ages and $\varepsilon_{Hf}(t)$, bulk-rock $\varepsilon_{Nd}(t)$, are given in Table 1.

3.1 Basong Tso cumulates

The diorite cumulates display adcumulate texture, dominated by coarse-grained amphibole and plagioclase plus minor intercumulus material of titanite, apatite and biotite (Fig. 2e–f). Sample TD17-9-3 has similar mineral assemblage to other diorite cumulate samples with much less titanite. The granodiorite cumulates display porphyritic texture, including plagioclase and amphibole interlocked with quartz plus interstitial biotite, titanite and apatite (Fig. 2g). Within both types of cumulates, most minerals are partially altered with plagioclase replaced by sericite, amphibole by epidote and biotite by chlorite (Fig. 2e–g).

3.2 Mamba granitoids

The host rocks of the Mamba batholith include granite and granodiorite, showing medium-grained equigranular texture. The granites mainly consist of quartz, K-feldspar and plagioclase with minor biotite, amphibole and Fe-oxides (Fig. 3e). The granodiorite has similar mineral assemblage to the granite with less quartz and more amphibole (Fig. 3f–g). Quartz monzodiorte MMEs share the same mineralogy as the host granodiorite but have less quartz and finer grain size (Fig. 3h). The MMEs show heteradcumulate texture with higher modal amphibole poikilitically enclosed in plagioclase and K-feldspar plus minor interstitial quartz, biotite, titanite, apatite and Fe-oxides (Fig. 3i).

4. Analytical methods and data

Analytical methods are given in Supplementary Text 1, including Cathodoluminescence (CL) images, mineral major elements, bulk-rock major and trace elements, Sr-Nd isotopes, zircon U-Pb dating and Hf isotopes.

4.1 Mineral compositions

Major element compositions for plagioclase and amphibole are given in Supplementary Table 1 and 2, respectively.

Plagioclase in the Basong Tso diorite and granodiorite cumulates has An = 28–49 (Fig. 4a). Plagioclase in the Mamba host rocks has varying composition with An = 13–46 (Fig. 4a), which is similar to that of the MMEs with An = 23–47 (Fig. 4a).

Amphibole is the dominant mafic mineral in all samples except for Mamba host sample T12-1-1. All amphibole is calcic with Ca_{Bsite} = 1.742–1.971 (Leake et al., 1997), but shows additional compositional variation, seeing Fig. 4b.

4.2 Bulk-rock major and trace element and Sr-Nd isotope data

Bulk-rock major element, trace element and Sr-Nd isotopic compositions of the studied samples are given in Supplementary Table 3.

Basong Tso cumulates

The diorite cumulates with low SiO_2 (47.6–51.2 wt.%) show linear trends (except for TiO_2) on SiO_2-variation diagrams (Figs. 5 and 6). The granodiorite cumulates have higher SiO_2 (59.8–60.7 wt.%) and limited range for other oxides (Fig. 6). The diorite cumulates are enriched in light rare earth elements (LREEs) relative to

heavy REEs (HREEs) with fractionated REE patterns and weak negative Eu anomalies (Fig. 7a). Most samples display positive Nb and Ta anomalies without negative Ti anomaly (except for sample TD17-9-3 with negative Nb, Ta and Ti anomalies in Fig. 7b, probably due to less titanite modes seeing 3.1 above). The granodiorite cumulates have similar REE patterns (Fig. 7c), but show negative U, Nb, Ta and Ti anomalies (Fig. 7d). Both types of cumulates have varying Nb/Ta of 12.43–24.12.

For diorite and granodiorite cumulates, their initial $^{87}Sr/^{86}Sr$ isotopic ratios and $\varepsilon_{Nd}(t)$ values are calculated at 190 and 200 Ma, respectively (using the zircon age data, see 4.3 below). The diorite cumulates have $(^{87}Sr/^{86}Sr)_i$ of 0.7059–0.7088 and $\varepsilon_{Nd}(t)$ of -1.69 to +1.97 (Fig. 8). The granodiorite cumulates have $(^{87}Sr/^{86}Sr)_i$ of 0.7061–0.7067 and lower $\varepsilon_{Nd}(t)$ of -5.95 to -4.90 (Fig. 8).

Mamba granitoids

The Mamba host rocks have varying SiO_2 (64.4–75.3 wt.%), equivalent to granodiorite and granite (Fig. 5a) and belonging to high-K calc-alkaline series with metaluminous characteristics (Fig. 5b–d). Their other major elements show variations inversely correlated with SiO_2 (Fig. 6a–e) (except for Na_2O, Fig. 6f). The MME has low SiO_2 (54.5 wt.%) with major element composition similar to that of the Basong Tso cumulates (Figs. 5b–d and 6).

The host rocks have enriched LREEs relative to HREEs with fractionated REE patterns (the most depleted HREEs are Ho and its neighbors with [Dy/Lu]n = 0.6–1.1) and weak negative Eu anomalies (Fig. 7e), and show significant negative Ba, Nb, Sr,

199 P and Ti anomalies (Fig. 7f). The MME has relatively higher middle and heavy REEs
200 than the host rocks, similar to the Basong Tso granodiorite cumulates (Fig. 7e–f).
201
202 **4.3 Zircon U-Pb age and Hf isotope**
203 LA-ICP-MS zircon U-Pb dating on nine samples and Hf isotope compositions of
204 eight samples are given in Supplementary Tables 4 and 5, respectively.
205 **Basong Tso cumulates**
206 Zircons from one diorite cumulate sample are euhedral short-prismatic with
207 varying size (~50–100 μm), exhibiting weak magmatic oscillatory zonation (Fig. 9a).
208 Analyzed spots give weighted mean $^{206}Pb/^{238}U$ age of 190±0.7 Ma (Fig. 10a). Their
209 thirteen Hf isotopic analyses give $\varepsilon_{Hf}(t) > 0$, ranging from +1.0 to +6.2 (Fig. 11).
210 Zircons from two granodiorite cumulate samples are euhedral prismatic with
211 varying size (~200–300 μm) and oscillatory zoning of magmatic origin (Fig. 9b and c).
212 Analyzed spots give weighted mean $^{206}Pb/^{238}U$ ages of 198±0.8 and 199±1 Ma (Fig.
213 10b and c). Their thirty-five Hf isotopic analyses give $\varepsilon_{Hf}(t) < 0$, ranging from -14.1 to
214 -3.8 (Fig. 11).
215 **Mamba granitoids**
216 Zircons from five host granite samples are similar to those of the Basong Tso
217 granodiorite cumulates (Fig. 9d–h). Analyzed spots give weighted mean $^{206}Pb/^{238}U$
218 ages of 194–189 Ma (Fig. 10d–h). Their sixty-two Hf isotopic analyses give varying
219 $\varepsilon_{Hf}(t)$ from -8.9 to +1.7 (Fig. 11).
220 Zircons from the MME sample are also of magmatic origin with varying size

(~50–200 μm) (Fig. 9i). Analyzed spots give weighted mean $^{206}Pb/^{238}U$ age of 190±2 Ma (Fig. 10i). Thirty-eight Hf isotopic analyses give varying $\varepsilon_{Hf}(t)$ from -3.0 to +3.7 (Fig. 11).

5. Discussion

5.1 Petrogenesis of the Early Jurassic igneous rocks in the central Lhasa subterrane

The age data on magmatic zircons from our samples indicate that the Basong Tso diorite and granodiorite cumulates crystallized at ca. 190 and 199–198 Ma, respectively; the Mamba MMEs formed coevally with their host rocks at ca. 190 and 194–189 Ma. We discuss the petrogenesis of these Early Jurassic igneous rocks respectively below.

5.1.1 Basong Tso cumulates

The Basong Tso rocks with typical cumulate textures (e.g., Schaen et al., 2018; Wager et al., 1960) are most consistent with an origin by crystal accumulation of amphibole, plagioclase and titanite from mafic andesitic magmas. Bulk-rock compositions of cumulate rocks are controlled by both compositions and modes of the constituent minerals (Niu et al., 2002a). Indeed, most major element oxides define trends between average compositions of plagioclase and amphibole, except for TiO_2 as the result of heterogeneous distribution of titanite (Fig. 6). Fig. 6a shows that the bulk-rock composition lies in space defined by titanite-plagioclase-amphibole assemblage. Moreover, the high Nb and Ta (Supplementary Table 3) and their

243 significant positive anomalies in Fig. 7 are consistent with high amphibole modes
244 (e.g., Tiepolo, et al., 2000). The high Nb/Ta (up to 24.12, Supplementary Table 3) is
245 also consistent with amphibole control because of $Kd_{Amp}^{Nb/Ta}$=1.40 (e.g., Foley et al.,
246 2002). Importantly, the major mineralogy of amphibole + plagioclase indicates that
247 their parental melts must be mafic andesitic magmas (e.g., Alonso-Perez et al., 2009;
248 Niu et al., 2013). Due to high viscosity, the crystal-melt separation is likely
249 incomplete. Thus, the Basong Tso granodiorite cumulates are likely crystal-rich
250 mixtures with trapped melt, but more samples and work are needed for a more
251 quantitative analysis.

252 **5.1.2 Mamba granitoids**

253 **Mamba host rocks**

254 With increasing viscosity in high-SiO_2 melt, crystal separation becomes more
255 ineffective. We suggest that the Mamba host rocks are melt-rich mixtures with
256 incompletely segregated crystals, which explain their major element compositional
257 systematics as a function of SiO_2 (Fig. 6a–e). These geochemical characteristics are
258 consistent with melt compositions of equilibrium crystallization experiment results of
259 hydrous andesite related to amphibole fractionation (Fig. 6, Alonso-Perez et al., 2009).
260 The amphibole fractional crystallization leads to reduction of TFeO, MgO and Dy/Yb
261 with increasing SiO_2 in the residual melt (Figs. 6c, d and 12a), and also results in
262 spoon-shaped REE patterns with variable and lower Tb, Dy, Ho and Er (Fig. 7e)
263 (amphibole preferentially incorporates middle REEs over heavy REEs; Davidson et
264 al., 2007). Meanwhile, fractional crystallization of plagioclase can effectively deplete

Al_2O_3, CaO, Eu (Figs. 6b, e and 12b) and Ba and Sr in the evolving magma (Fig. 7f). Therefore, the Mamba host rock compositional systematics are consistent with andesitic magmas that have undergone amphibole-plagioclase fractional crystallization.

Mamba MME

Controversy exists on the MME petrogenesis, including foreign xenoliths (e.g., Vernon, 1983), partial melting residues of the source rocks (e.g., Chappell et al., 1987), magma mixing between mantle-derived basaltic magma and crust-derived felsic magma (e.g., Didier, 1987), and earlier cumulate crystallized from the same magmatic system (e.g., Donaire et al., 2005). In this study, the Mamba MME sample has typical magmatic textures in both field and petrographic observations without peraluminous minerals (Fig. 3d, h, i) and formed coevally with their host rocks (Table 1), ruling out the foreign xenolith and restite origins. For MMEs formed by magma mixing, there are some common characteristics, (1) distinguishable isotopic contrast between the MMEs and the host rocks; (2) disequilibrium textures of the MMEs, e.g., complex zoning of clinopyroxene (e.g., Wang et al., 2013) or reversed zoning of plagioclase (e.g., Shcherbakov et al., 2011). However, none of the above typical evidence for magma mixing is observed. Instead, the MMEs have cumulate textures, and their bulk-rock compositions are mainly controlled by those of amphibole-plagioclase (Figs. 6). Moreover, the MMEs and their host rocks have the same mineral assemblage, similar mineral (plagioclase and amphibole) compositions and overlapping zircon $\varepsilon_{Hf}(t)$ values (Figs. 3h, 4 and 11). Therefore, the MMEs represent earlier cumulate

derived from cogenetic magma with their host rocks.

5.2 Constraints on the source

The Early Jurassic cumulates (Basong Tso cumulates and Mamba MME) in the CLT comprise dominantly amphibole and plagioclase that are common cumulate crystals of andesitic melts, whereas the typical cumulate from evolved basaltic melt would be gabbro dominated by clinopyroxene and plagioclase (Niu et al., 2013). Moreover, the compositions of the Mamba host granitoids are consistent with melt compositions of equilibrium crystallization experiment results of hydrous andesite (Fig. 6, Alonso-Perez et al., 2009). Thus, the primary magmas parental to the studied Early Jurassic igneous rocks are mafic andesite. In addition, our bulk-rock $\varepsilon_{Nd}(t)$ (-5.95 to +1.97) and zircon $\varepsilon_{Hf}(t)$ (-14.1 to +6.2) isotopic data indicate significant mantle or juvenile mafic crust contribution to the granitoid magmatism. Moreover, the positive correlation of La/Sm with SiO_2 (Fig. 12c) further indicates crustal assimilation to be important, which is understood to be inevitable in terms of crustal melting or magma chamber processes. Generally, the source for the andesitic parental magmas with mantle isotopic signature could be (1) evolved mantle-derived basaltic magmas; (2) juvenile mafic continental crust derived from the mantle in no distant past; and possibly (3) the underplated ocean crust. Firstly, it is inadequate to produce huge granitoid batholiths, such as the Mamba batholith, through basaltic magma evolution. Moreover, no related juvenile mafic continental rocks have been reported so far, except for ca. 492 Ma basalts with negative bulk-rock $\varepsilon_{Nd}(t)$ in the CLT (Zhu et al., 2012). Therefore, we suggest, until now, the most likely source for the andesitic

magma parental to the studied Early Jurassic igneous rocks is partial melting of the remaining Late Paleozoic Sumdo Tethyan ocean crust represented by the Sumdo eclogite that had exhumated to the middle-lower crust at ca. 200 Ma (e.g., Cheng et al., 2015). The remaining ocean crust could undergo partial melting to produce andesitic melt under amphibolite-facies conditions (cf. Niu et al., 2013 and references therein). Moreover, the coeval metamorphic conditions (9 kbar at ca. 204–192 Ma, Weller et al., 2015) of the country rocks indicated that the magmas parental to the Basong Tso cumulates were formed at the middle-lower crustal depths. This possibility has also been suggested by Zhu et al. (2011).

The model of partial melting of the remaining ocean crust and the recycled terrigenous sediments has been proposed and tested by Niu and co-workers in many orogenic belts (e.g., Chen et al., 2016; Huang et al., 2014; Mo et al., 2008; Niu et al., 2013). As we known, the very geodynamic trigger for the Early Mesozoic magmatism of the Lhasa terrane is the northward subduction of the Neo-Tethyan seafloor beneath the Lhasa terrane (e.g., Chu et al., 2006; Ji et al., 2009; Zhang et al, 2007b). During seafloor subduction, mantle wedge flow supplies heat and maintains to heat the underplated hydrated ocean crust and related continental material that would melt together to generate the andesitic magmas parental to the studied Early Jurassic igneous rocks with inherited mantle isotopic signatures.

5.3 Late Triassic–Early Jurassic magmatism of the Lhasa terrane

The Late Triassic–Early Jurassic magmatic rocks are widely scattered in the entire SLT and central–eastern CLT (Fig. 1b). In the SLT, the Early Mesozoic

magmatic rocks include plutonic and volcanic rocks. The plutonic rocks mainly consist of diorite, tonalite, granodiorite and granite with minor hornblende gabbro, and their bulk-rock geochemical data are characterized by medium-K calc-alkaline and metaluminous, typical of I-type granitoids with zircon $\varepsilon_{Hf}(t) > 0$ (e.g., Guo et al., 2013; Meng et al., 2016a, b; Shui et al., 2018; Xu et al., 2019; Zhu et al., 2011). In the CLT, the Early Mesozoic magmatic rocks occur as batholiths in the eastern CLT and plutons in the central CLT (Fig. 1b). The batholiths near Mamba, Sumdo and Jinda areas are I-type granodiorite and granite with MMEs, compositionally medium- to high-K calc-alkaline and metaluminous, with variable zircon $\varepsilon_{Hf}(t)$ values (He et al., 2005, 2006; Yu et al., 2018; Zhu et al., 2011; this study). By comparison, the plutons near Luoza and Ningzhong areas mainly consist of peraluminous S-type granite with zircon $\varepsilon_{Hf}(t) < 0$ (Chu et al., 2006; Liu et al., 2006; Zhang et al., 2007b).

5.4 Crustal evolution of the Lhasa terrane

The crust in the Lhasa terrane has been considered to be dominated by ancient crust in the CLT, but dominated by younger juvenile crust in the SLT and NLT as manifested by zircon Hf and bulk-rock Nd isotope compositions of the granitoids (e.g., Hou et al., 2015; Zhu et al., 2011). Zircon Hf isotope has been used as a useful tool for understanding continental crust formation and evolution (e.g., Kinny and Mass, 2003). Here we show zircon $\varepsilon_{Hf}(t)$ values from the Early Mesozoic plutonic rocks (~215–170 Ma) in the SLT and CLT. Fig. 11 shows that granitoids from the SLT have zircon $\varepsilon_{Hf}(t) > 0$, whereas granitoids in the CLT have zircon $\varepsilon_{Hf}(t)$ varying systematically from $\varepsilon_{Hf}(t) < 0$ at ca. 210 Ma towards $\varepsilon_{Hf}(t) > 0$ at ca. 195 Ma. Spatially,

353 from north to south, zircon $\varepsilon_{Hf}(t)$ values gradually increase, i.e., from $\varepsilon_{Hf}(t) < 0$ in the
354 CLT to $\varepsilon_{Hf}(t) > 0$ southward in Fig. 13. It is well understood that crust–mantle
355 interaction is inevitable during source melting (e.g., melting of subducted sediments)
356 and magma emplacement (e.g., crustal assimilation).

357 Here, we suggest that although mantle material contribution (juvenile or
358 remelting of mantle-derived rocks) is important, significant melt assimilation with
359 ancient crustal material results in the signature of $\varepsilon_{Hf}(t) < 0$ in the northernmost CLT
360 in the Late Triassic, then melting of abundant recycled terrigenous sediments of upper
361 continental crust and remaining of the Sumdo Tethyan ocean crust in the melting
362 region generates the andesitic magma parental to the ca. 200 Ma granodiorite
363 cumulates (Fig. 14a). With the CLT magmatism getting younger and southward,
364 melting of much more Sumdo Tethyan ocean crust with adjacent ancient lower crust
365 forms the parental magmas of the ca. 190 Ma diorite cumulates and MME-bearing
366 granitoid, when the zircon $\varepsilon_{Hf}(t)$ gradually increases towards positive values,
367 reflecting increasing mantle contribution (Fig. 14b). Notedly, zircon $\varepsilon_{Hf}(t)$ of the
368 granitoids from the CLT are all negative at longitude 88.6−90.6° E (Fig. 13b), which
369 is consistent with S-type granitoids of crustal re-working origin (see above 5.3). For
370 the coeval plutonic rocks of the SLT, zircon Hf isotope also shows signatures of the
371 crustal assimilation, representing the wide range of zircon $\varepsilon_{Hf}(t)$ at ca. 205−200 Ma
372 (Fig. 11) and values around zero at latitude ca. 29.7° N (Fig. 13a and c). Our study
373 supports Zhu et al. (2011) that granitoids from the SLT are dominated by mantle
374 contributions up to 50–90%, but those from the CLT has much less mantle

375 contribution (0–60 %) (Fig. 8). Ma et al. (2019) recently showed that the SLT already
376 experienced growth process of juvenile crust during the Paleozoic and was once a
377 microcontinent with Precambrian basement but transformed into juvenile terrane over
378 time. We suggest that the crustal evolution is a multi-episode and gradual process. For
379 the CLT, the multiple plutonic rocks record the Early Mesozoic crustal evolution with
380 increasing mantle contribution with time as manifested by increasing zircon $\varepsilon_{Hf}(t)$
381 values.
382
383 **6. Conclusion**
384 (1) The Early Jurassic igneous rocks in the CLT include the Basong Tso plutons of
385 diorite cumulate (ca. 190 Ma), granodiorite cumulate (ca. 200 Ma) and the
386 Mamba batholith of host granitoids and MMEs with the same crystallization age
387 (~190 Ma).
388 (2) The Basong Tso plutons are formed by crystal accumulation of amphibole,
389 plagioclase and titanite from a mafic andesitic magma. The Mamba host
390 granitoids are formed through amphibole-plagioclase fractional crystallization of
391 an andesitic magma. The MMEs share the same mineralogy and indistinguishable
392 isotopic compositions with their host granitoids, indicating earlier cumulate from
393 the same magmatic system as their host rocks.
394 (3) The parental magma for the Early Jurassic igneous rocks with inherited mantle
395 isotopic signatures is best understood as resulting from partial melting of the
396 hydrated ocean crust together with varying continental material.

(4) The multiple plutonic rocks (~215–170 Ma) in the CLT record the Early Mesozoic crustal evolution of the Lhasa terrane, characterized by increasing mantle contribution reflected by gradual increase of zircon $\varepsilon_{Hf}(t)$ with time. The SLT had already experienced juvenile crustal growth in the Paleozoic.

Acknowledgement

We want to thank two anonymous journal referees and Editor-in-Chief Xian-Hua Li for their constructive comments, which clearly help improve the quality of this paper. This study was co-supported by the National Key Research and Development Project of China (2016YFC0600310), the National Natural Science Foundation of China (grant 41872070 and 91855210) and the China Geological Survey (grant DD20190057). Xin Dong acknowledges the China Scholarship Council for funding a 12-month research at Durham University, UK (CSC NO. 201809110024). We thank Dr. Yanhao Lin, Zhijia Chen, Huixia Ding and Yanfei Chen, PhD. student Shengkai Qin for taking part in field work.

References

Alonso-Perez R., Müntener O., Ulmer P., 2009. Igneous garnet and amphibole fractionation in the roots of island arcs: experimental constraints on andesitic liquids. Contributions to Mineralogy and Petrology 157, 541–558.

Ben Othman, D., Polve, M., Allegre, C.J., 1984. Nd-Sr isotopic composition of granulites and constraint on the evolution of the lower continental crust. Nature

307, 510–515.

Chappell, B., White, A., Wyborn, D., 1987. The importance of residual source material (restite) in granite petrogenesis. Journal of Petrology 28, 1111–1138.

Chen, S., Niu, Y.L., Li, J.Y., Sun, W.L., Zhang, Y., Hu, Y., Shao, F.L., 2016. Syn-collisional adakitic granodiorites formed by fractional crystallization: insights from their enclosed mafic magmatic enclaves (MMEs) in the Qumushan pluton, North Qilian Orogen at the northern margin of the Tibetan Plateau. Lithos 248–251, 455–468.

Cheng, H., Liu, Y., Vervoort, J.D., Lu, H., 2015. Combined U-Pb, Lu-Hf, Sm-Nd and Ar-Ar multichronometric dating on the Bailang eclogite constrains the closure timing of the Paleo-Tethys Ocean in the Lhasa terrane, Tibet. Gondwana Research 28, 1482–1499.

Chu, M.F., Chung, S.L., Song, B., Liu, D.Y., O'Reilly, S.Y., Pearson, N.J., Ji, J.Q. Wen, D.J., 2006. Zircon U-Pb and Hf isotope constraints on the Mesozoic tectonics and crustal evolution of southern Tibet. Geology 34, 745–748.

Davidson, J., Turner, S., Handley, H., Dosseto, A., 2007. Amphibole "sponge" in arc crust? Geology 35, 787–790.

Deer, W.A., Howie, R.A., Zussman, J., 1992. An Introduction to the Rock-Forming Minerals. 2nd Edition. Harlow: Longman Group. pp. 1–232.

Dewey, J. F., Shackleton, R. M., Chang, C., Sun, Y., 1988. The tectonic evolution of the Tibetan Plateau. Philosophical Transactions of the Royal Society of London, Series A 327, 379–413.

441 Didier, J., 1987. Contribution of enclave studies to the understanding of origin and
442 evolution of granitic magmas. Geologische Rundschau 76, 41–50.
443 Donaire, T., Pascual, E., Pin, C., Duthou, J.L., 2005. Microgranular enclaves as
444 evidence of rapid cooling in granitoid rocks: the case of the Los Pedroches
445 granodiorite, Iberian Massif, Spain. Contributions to Mineralogy and Petrology
446 149, 247–265.
447 Dong, X., Zhang, Z.M., Santosh, M., 2010. Zircon U–Pb chronology of the Nyingtri
448 Group, Southern Lhasa Terrane, Tibetan Plateau: implications for Grenvillian
449 and Pan-African provenance and Mesozoic-Cenozoic metamorphism. The
450 Journal of Geology 118, 677–690.
451 Dong, X., Zhang, Z.M., Santosh, M., Wang, W., Yu, F., Liu, F., 2011a. Late
452 Neoproterozoic thermal events in the northern Lhasa terrane, south Tibet:
453 Zirconchronology and tectonic implications. Journal of Geodynamics 52, 389–
454 405.
455 Dong, X., Zhang, Z.M., Liu, F., Wang, W., Yu, F., Shen, K., 2011b. Zircon U–Pb
456 geochronology of the Nyainqêntanglha Group fromthe Lhasa terrane: new
457 constraints on the Triassic orogeny of the south Tibet. Journal of Asian Earth
458 Sciences 42, 732–739.
459 Dong, X., Zhang, Z.M., 2013. Genesis and tectonic significance of the Early Jurassic
460 magmatic rocks from the southern Lhasa terrane. Acta Petrologica Sinica 29,
461 1933–1948 (in Chinese with English abstract).
462 Dong, X., Zhang, Z.M., Liu, F., He, Z.Y., Lin, Y.H., 2014. Late Paleozoic intrusive

rocks from the southeastern Lhasa terrane, Tibetan Plateau, and their Late Mesozoic metamorphism and tectonic implications. Lithos 198–199, 249–262.

Dong, X., Zhang, Z.M., Niu, Y.L., Tian, Z.L., Zhang, L.L., 2020. Reworked Precambrian metamorphic basement of the Lhasa terrane, southern Tibet: Zircon/Titanite U–Pb geochronology, Hf isotope and Geochemistry. Precambrian Research 336, 105496

Faure, G., 1977. Principles of isotope geology. John Wiley and Sons, USA.

Foley, S., Tiepolo, M., Vannucci, R., 2002. Growth of early continental crust controlled by melting of amphibolite in subduction zones. Nature 417, 837–840.

Guo, L.S., Liu, Y.L., Liu, S.W., Cawood, P.A., Wang, Z.H. Liu, H.F., 2013. Petrogenesis of Early to Middle Jurassic granitoid rocks from the Gangdese belt, Southern Tibet: implications for early history of the Neo-Tethys. Lithos 179, 320–33.

Harris, N.B.W., Holland, T.J.B., Tindle, A.G., 1988a. Metamorphic rocks of the 1985 Tibet Geotraverse, Lhasa to Golmud. Philosophical Transactions of the Royal Society of London, Series A 327, 203–213.

Harris, N.B.W., Xu, R.H., Lewis, C.L., Hawkesworth, C.L., Zhang, Y.Q., 1988b. Isotope geochemistry of the 1985 Tibet Geotraverse, Lhasa to Golmud. Philosophical Transactions of the Royal Society of London, Series A 327, 263–285.

He, Z.H., Yang, D.M., Zheng, C.Q., Huang, Y.C., 2005. Geochemistry of the Indosinian granitoids in the Mamba area, Gangdise belt, Tibet and its tectonic

significance. Geological Bulletin of China 24, 354–359 (in Chinese with English abstract).

He, Z.H., Yang, D.M., Zheng, C.Q., Wang, T.W., 2006. Isotopic dating of the Mamba granitoid in the Gangdise tectonic belt and its constraint on the subduction time of the Neotethys. Geological review 52, 100–106 (in Chinese with English abstract).

Hou, Z.Q., Duan, L., Lu, Y.J., Zheng, Y.C., Zhu, D.C., Yang, Z.M., Yang, Z.S., Wang, B.D., Pei, Y.R., Zhao, Z.D., McCuaig, T.C., 2015. Lithospheric architecture of the Lhasa terrane and its control on ore deposits in the Himalayan–Tibetan orogen. Economic Geology 110, 1541–1575.

Huang, H., Niu, Y.L., Nowell G., Zhao, Z.D., Yu, X.H., Zhu, D.C., Mo, X.X., Ding, S., 2014. Geochemical constraints on the petrogenesis of granitoids in the East Kunlun Orogenic belt, northern Tibetan Plateau: implications for continental crust growth through syn-collisional felsic magmatism. Chemical Geology 370, 1–18.

Irvine, T.N, Barager, W.R.A., 1971. A guide to the chemical classification of the common volcanic rocks. Canadian Journal of Earth Sciences 8, 523–548.

Jagoutz, O., Kelemen, P.B., 2015. Role of Arc Processes in the Formation of Continental Crust. Annual Review of Earth and Planetary Sciences 43, 363–404.

Ji, W.Q., Wu, F.Y., Chung, S.L., Li, J.X., Liu, C.Z., 2009. Zircon U-Pb geochronology and Hf isotopic constraints on petrogenesis of the Gangdese batholith, southern Tibet. Chemical Geology 262, 229–245.

Ji, W.Q., Wu, F.Y., Liu, C.Z., Chung, S.L., 2012. Identification of early Carboniferous granitoids from southern Tibet and implications for terrane assembly related to the Paleo-Tethyan evolution. The Journal of Geology 120, 531–541.

Kapp, J.L.D., Harrison, T.M., Kapp, P., Grove, M., Lovera, O.M., Lin, D., 2005. Nyainqentanglha Shan: a window into the tectonic, thermal, and geochemical evolution of the Lhasa block, southern Tibet. Journal of Geophysical Research Solid Earth 110, B08413, doi:10.1029/2004JB003330, 2005.

Kinny, P.D., Maas, R., 2003. Lu-Hf and Sm-Nd Isotope Systems in Zircon, in Zircon, reviews in mineralogy and geochemistry, ed. J. M. Hanchar and P. W. O. Hoskin, vol. 53, pp. 327–341.

Lang, X.H., Tang, J.X., Li, Z.J., Huang, Y., Ding, F., Yang, H.H., Xie, F.W., Zhang, L., Wang, Q. Zhou, Y., 2014a. U-Pb and Re-Os geochronological evidence for the Jurassic porphyry metallogenic event of the Xiongcun district in the Gangdese porphyry copper belt, southern Tibet, PRC. Journal of Asian Earth Sciences 79, 608–622.

Lang, X.H., Tang, J.X., Xie, F.W., Li, Z.J., Huang, Y., Ding, F., Yang, H.H., Zhou, Y., Wang, Q., 2014b. Geochronology and geochemistry of the southern porphyry in the Xiongcun district and its geological implications, Tibet. Geotectonica Et Metallogenia 38, 609–620 (in Chinese with English abstract).

Le Bas, M.J., Streckeisen, A.L., 1991. The IUGS systematics of igneous rocks. Journal of the Geological Society 148, 825–833.

Leake, B.E., Woolley, A.R., Arps, C.E.S., other 19 co-authors, 1997. Nomenclature of

amphiboles: report of the subcommittee on amphiboles of the International Mineralogical Association. Commission on New Minerals and Mineral Names. The Canadian Mineralogist 35, 219–246.

Li, H.Q., Xu, Z.Q., Yang, J.S., Cai, Z.H., Chen, S.Y., Tang, Z.M., 2009. Records of Indosinian orogenesis in Lhasa Terrane, Tibet. Journal of Earth Science 20, 348–363.

Li, C., Wu, Y.W., Wang, M., Yang, H.T., 2010. Significant progress on Pan-African and Early Paleozoic orogenic events in Qinghai–Tibet Plateau: discovery of Pan-African orogenic unconformity and Cambrian System in the Gangdese area, Tibet, China. Geological Bulletin of China 29, 1733–1736 (in Chinese with English Abstract).

Li, P., 1955. Primary understanding of geology, eastern Tibet. Chinese Science Bulletin 7, 62–71 (in Chinese).

Li, Z.L., Yang, J.S., Xu, Z.Q., Li, T.F., Xu, X.Z., Ren, Y.F., Robinson, O.T., 2009. Geochemistry and Sm-Nd and Rb-Sr isotopic composition of eclogite in the Lhasa terrane, Tibet, and its geological significance. Lithos 109, 240–247.

Lin, Y.H., Zhang, Z.M., Dong, X., Xiang, H., Yan, R., 2013, Early Mesozoic metamorphism and tectonic significance of the eastern segment of the Lhasa terrane, south Tibet. Journal of Asian Earth Science 78, 160–183.

Liu, Q.S., Jiang, W., Jian, P., Ye, P.S., Wu, Z.H., Hu, D.G., 2006. Zircon SHRIMP U-Pb age and petrochemical and geochemical features of Mesozoic muscovite monzonitic granite at Ningzhong, Tibet. Acta Petrologica Sinica 22; 643–652 (in

Chinese with English Abstract).

Ma, L., Kerr, A.C., Wang, Q., Jiang, Z.Q., Tang, G.J., Yang, J.H., Xia, X.P., Hu, W.L., Yang, Z.Y., Sun, P., 2019. Nature and evolution of crust in southern Lhasa, Tibet: Transformation from microcontinent to juvenile terrane. Journal of Geophysical Research: Solid Earth 124, 6452–6474.

Ma, S.W., Meng, Y.K., Xu, Z.Q., Liu, X.J., 2017. The discovery of late Triassic mylonitic granite and geologic significance in the middle Gangdese batholiths, southern Tibet. Journal of Geodynamics 104, 49–64.

Ma, X.X., Meert, J.G., Xu, Z.Q. Yi, Z.Y., 2018. Late Triassic intra-oceanic arc system within Neotethys: evidence from cumulate appinite in the Gangdese belt, southern Tibet. Lithosphere 10, 545–565.

Meng, F.Y., Zhao, Z., Zhu, D.C., Mo, X.X., Guan, Q., Huang, Y., Dong, G.C., Zhou, S., DePaolo, D.J., Harrison, T.M., Zhang, Z.C., Liu, J.L., Liu, Y.S., Hu, Z.C., Yuan, H.L., 2014, Late Cretaceous magmatism in Mamba area, central Lhasa subterrane: products of back-arc extension of Neo-Tethyan Ocean? Gondwana Research 26, 505–520.

Meng, Y.K., Xu, Z.Q., Santosh, M., Ma, X.X., Chen, X.J., Guo, G.L. Liu, F., 2016a. Late Triassic crustal growth in southern Tibet: evidence from the Gangdese magmatic belt. Gondwana Research 37, 449–464.

Meng, Y.K., Dong, H.W., Cong, Y., Xu, Z.Q. Cao, H., 2016b. The early-stage evolution of the Neo-Tethys ocean: evidence from granitoids in the middle Gangdese batholith, southern Tibet. Journal of Geodynamics 94–95, 34–49.

573 Mo, X.X., Niu, Y.L., Dong, G.C., Zhao, Z.D., Hou, Z.Q., Zhou, S., Ke, S., 2008.
574 Contribution of syncollisional felsic magmatism to continental crust growth: a
575 case study of the Paleogene Linzizong volcanic Succession in southern Tibet.
576 Chemical Geology 250, 49–67.
577 Niu, Y.L., Gilmore, T., Mackie, S., Greig, A., Bach, W., 2002a. Mineral chemistry,
578 whole-rock compositions, and petrogenesis of Leg 176 gabbros: data and
579 discussion. In Natland, J.H., et al. (Eds), Proceedings of the Ocean Drilling
580 Program Scientific Results 176, pp. 1–69.
581 Niu, Y.L, Regelous, M., Wendt, J.I., Batiza, R., O'Hara, M.J., 2002b. Geochemistry of
582 near-EPR seamounts: importance of source vs. process and the origin of enriched
583 mantle component, Earth and Planetary Science Letters 199, 327–345.
584 Niu, Y.L., O'Hara, 2003. Origin of ocean island basalts: a new perspective from
585 petrology, geochemistry, and mineral physics considerations. Journal of
586 Geophysical Resarch, 108, 2209, doi:10.1029/2002JB002048, 2003.
587 Niu, Y.L., Zhao, Z.D., Zhu, D.C., Mo, X.X., 2013. Continental collision zones are
588 primary sites for net continental crust growth—a testable hypothesis.
589 Earth-Science Reviews 127, 96–110.
590 Pan, G.T., Ding, J., Yao, D., Wang, L., 2004. Geological Map of the Qinghai–Xizang
591 (Tibet) Plateau and Adjacent Areas. Chengdu Cartographic Publishing House,
592 Chengdu (in Chinese).
593 Peccerillo, R., Taylor, S.R., 1976. Geochemistry of eocene calc-alkaline volcanic
594 rocks from the Kastamonu area, Northern Turkey. Contributions to Mineralogy

and Petrology 58, 63–81.

Qu, X.M., Xin, H.B. Xu, W.Y., 2007. Collation of age of ore-hosting volcanics in Xiongcun superlarge Cu-Au deposit on basis of three zircon U-Pb SHRIMP ages. Mineral Deposits 26, 512–518 (in Chinese with English abstract).

Rudnick, R.L., Gao, S., 2003. Composition of the continental crust. In Treatise on Geochemistry, vol. 3 (ed. R. L. Rudnick). The Crust. Elsevier. pp. 1–64.

Rudnick, R.L., 1995. Making continental crust. Nature 378, 571.

Schaen, A.J., Singer, B.S., Cottle, J.M., Garibali, N., Schoene, B., Satkoski, A.M. Fournelle, J., 2018. Textural and mineralogical record of low-pressure melt extraction and silicic cumulate formation in the late Miocene Risco Bayo–Huemul plutonic complex, southern Andes. Journal of Petrology 59, 1991–2016.

Shcherbakov, V.D., Plechov, P.Y., Izbekov, P.E., Shipman, J.S., 2011. Plagioclase zoning as an indicator of magma processes at bezymianny volcano, kamchatka. Contributions to Mineralogy and Petrology 162, 83–99.

Shui, X.F., He, Z.Y., Zhang, Z.M., Lu, T.Y., 2016. Magma origin of Early Jurassic tonalites in the Eastern Gangdese Magmatic Belt, southern Tibet and its implications for the crustal evolution of the Lhasa Terrane. Acta Geologica Sinica 90, 3129–3152 (in Chinese with English abstract).

Shui, X.F., He, Z.Y., Klemd, R., Zhang, Z.M., Lu, T.Y. Yan, L.L., 2018. Early Jurassic adakitic rocks in the southern Lhasa sub-terrane, southern Tibet: petrogenesis and geodynamic implications. Geological Magazine 155, 132–148.

Tafti, R., Mortensen, J.K., Lang, J.R., Rebagliati, M. Oliver, J.L., 2009. Jurassic U-Pb

and Re-Os ages for the newly discovered Xietongmen Cu-Au porphyry district, Tibet, PRC: implications for metallogenic epochs in the southern Gangdese belt. Economic Geology 104, 127–136.

Tafti, R., Lang, J.R., Mortensen, J.K., Oliver, J.L. Rebagliati, C.M., 2014. Geology and geochronology of the Xietongmen (Xiongcun) Cu-Au porphyry district, Southern Tibet, China. Economic Geology 109, 1967–2001.

Tan, C.C., 2012. The age and petrogenesis of the Dongga intrusion in the Gangdese magmatic belt, north Xigaze. (Master thesis). China University of Geosciences, Beijing. pp. 1–73 (in Chinese with English abstract).

Tang, J.X., Li, F.J., Li, Z.J., Zhang, L., Tang, X.Q., Deng, Q., Lang, X.H., Huang, Y., Yao, X.F., Wang, Y., 2010. Period of time for the formation of main geologic bodies in Xiongcun copper-gold deposit, Xietongmen County, Tibet: evidence from Zircon U-Pb ages and Re-Os ages of molybdenite. Mineral Deposits 29, 461–475 (in Chinese with English abstract).

Taylor, S.R., McLennan, S.M., 1985. The Continental Crust: its Composition and Evolution. Blackwell, Oxford, pp. 312.

Tiepolo, M., Vannucci, R., Oberti, R., Foley, S., Bottazzi, P., Zanetti, A., 2000. Nb and Ta incorporation and fractionation in titanian pargasite and kaersutite: crystal-chemical constraints and implications for natural systems. Earth and Planetary Science Letters 176, 185–201.

Vernon, R.H., 1983. Restite, xenoliths and microgranitoid enclaves in granites. Journal and Proceedings of the Royal Society of New South Wales 116, 77–103.

639 Wager, L.R., Deer, W.A., 1939. Geological investigation in East Greenland, Part III,
640 The petrology of the Skaergaard intrusion, Kangerdluqssuaq, East Greenland.
641 Meddelser om Gronland 105.
642 Wager, L.R., Brown, G.M., Wansworth, W.J., 1960. Types of igneous cumulates.
643 Journal of Petrology 1, 73–85.
644 Wang, Q., Li, X.H., Jia, X.H.,Wyman, D., Tang, G.J., Li, Z.X.,Ma, L., Yang, Y.H.,
645 Jiang, Z.Q., Gou, G.N., 2013. Late Early Cretaceous adakitic granitoids and
646 associated magnesian and potassium-rich mafic enclaves and dikes in the
647 Tunchang–Fengmu area, Hainan Province (South China): partial melting of
648 lower crust and mantle, and magma hybridization. Chemical Geology 328, 222–
649 243.
650 Wang, R., Tafti, R., Hou, Z.Q., Shen, Z.C., Guo, N., Evans, N.J., Jeon, H., Li, Q.Y. Li,
651 W.K. 2017a. Across-arc geochemical variation in the Jurassic magmatic zone,
652 Southern Tibet: implication for continental arc-related porphyry Cu-Au
653 mineralization. Chemical Geology 451, 116–134.
654 Wang, R.Q., Qiu, J.S., Yu, S.B., Zhao, J.L., 2017b. Crust-mantle interaction during
655 Early Jurassic subduction of Neo-Tethyan oceanic slab: evidence from the
656 Dongga gabbro-granite complex in the southern Lhasa subterrane, Tibet. Lithos
657 292–293, 262–277.
658 Weller, O.M., St-Onge, M.R., Searle, M.P., Waters, D.J., Rayner, N., Chen, S., Chung,
659 S.L., Palin, R.M., 2015. Quantifying the *P–T–t* conditions of north-south Lhasa
660 terrane accretion: new insight into the pre-Himalayan architecture of the Tibetan

plateau. Journal of Metamorphic Geology 33, 91–113.

Xu, B., Hou, Z.Q., Zheng, Y.C., Wang, R., He, M.Y., Zhou, L.M., Wang, Z.X., He, W.Y., Zhou, Y., Yang, Y., 2017a. In situ elemental and isotopic study of diorite intrusions: implication for Jurassic arc magmatism and porphyry Cu-Au mineralization in southern Tibet. Ore Geology Reviews 90, 1063–1077.

Xu, B., Hou, Z.Q., Zheng, Y.C., Zhou, Y., Zhou, L.M., Yang, Y., Han, Y.W., Zhen, G., Wu, C.D., 2017b. Jurassic Hornblende Gabbros in Dongga, Eastern Gangdese, Tibet: partial Melting of Mantle Wedge and Implications for Crustal Growth. Acta Geologica Sinica 91, 545–564.

Xu, W., Zhu, D.C., Wang, Q., Weinberg, R.F., Wang, R., Li, S.M., Zhang, L.L., Zhao, Z.D., 2019. Constructing the early mesozoic gangdese crust in southern Tibet by hornblende-dominated magmatic differentiation. Journal of Petrology. doi: 10.1093/petrology/egz005

Yang, J.S., Xu, Z.Q., Li, Z.L., Xu, X.Z., Li, T.F., Ren, Y.F., Li, H.Q., Chen, S.Y., Robinson, P.T., 2009. Discovery of an eclogite belt in the Lhasa block, Tibet: a new border for Paleo-Tethys? Journal of Asian Earth Science 34, 76–89.

Yang, Z.M., Hou, Z.Q., Xia, D.X., Song, Y.C., Li, Z., 2008. Relationship between western porphyry and mineralization in Qulong copper deposit of Tibet and its enlightenment to further exploration. Mineral Deposits 27, 28–36 (in Chinese with English abstract).

Yang, Z.M., Hou, Z.Q., Jiang, Y.F., Zhang, H.R., Song, Y.C., 2011. Sr-Nd-Pb and zircon Hf isotopic constraints on petrogenesis of the Late Jurassic granitic

porphyry at Qulong, Tibet. Acta Petrologica Sinica 27, 2003–2010 (in Chinese with English abstract).

Yin, A., Harrison, T. M., 2000. Geologic evolution of the Himalayan-Tibetan orogen. Annual Review of Earth and Planetary Sciences 28, 211–280.

Yu, Y.P., Xie, C.M., Fan, J.J., Wang, M., Dong, Y.C., Wang, B., Hao, Y.J., 2018. Zircon U–Pb geochronology and geochemistry of Early Jurassic granodiorites in Sumdo area, Tibet: constraints on petrogenesis and the evolution of the Neo-Tethyan Ocean. Lithos 320–321, 134–143.

Zeng, L.S., Liu, J., Gao, L.E., Chen, F.Y., Xie, K.J., 2009. Early Mesozoic high-pressure metamorphism within the Lhasa block, Tibet and implications for regional tectonics. Earth Science Frontiers 16, 140–151.

Zhang, H.F., Xu, W.C., Guo, J.Q., Zong, K.Q., Cai, H.M., Yuan, H.L., 2007a. Indosinian orogenesis of the gangdise terrane: evidences from zircon U-Pb dating and petrogenesis of granitoids. Earth Science –Journal of China University of Geoscience 32, 155–66 (in Chinese with English abstract).

Zhang, H.F., Xu, W.C., Guo, J.Q., Zong, K.Q., Cai, H.M. Yuan, H.L., 2007b. Zircon U-Pb and Hf isotopic composition of deformed granite in the southern margin of the Gangdese belt, Tibet: evidence for early Jurassic subduction of Neo-Tethyan oceanic slab. Acta Petrologica Sinica 23, 1347–1353 (in Chinese with English abstract).

Zhang, Z.M., Dong, X., Liu, F., Lin, Y.H., Yan, R., He, Z.Y., Santosh, M., 2012. The making of Gondwana: discovery of 650 Ma HP granulites from the North Lhasa,

Tibet. Precambrian Reseach 212–213, 107–116.

Zhu, D.C., Pan, G.T., Chung, S.L., Liao, Z.L., Wang, L.Q., Li, G.M., 2008. SHRIMP zircon age and geochemical constraints on the origin of Early Jurassic volcanic rocks from the Yeba Formation, southern Gangdese in south Tibet. International Geology Review 50, 442–471.

Zhu, D.C., Mo, X.X., Niu, Y., Zhao, Z.D., Wang, L.Q., Pan, G.T., Wu, F.Y., 2009. Zircon U-Pb dating and in-situ Hf isotopic analysis of Permian peraluminous granite in the Lhasa terrane, southern Tibet: implications for Permian collisional orogeny and paleogeography. Tectonophysics 469, 48–60.

Zhu, D.C., Zhao, Z.D., Niu, Y.L., Mo, X.X., Chung, S.L., Hou, Z.Q., Wang, L.Q., Wu, F.Y., 2011. The Lhasa Terrane: record of a microcontinent and its histories of drift and growth. Earth and Planetary Science Letters 301, 241–255.

Zhu, D.C., Zhao, Z.D., Niu, Y.L., Dilek, Y., Wang, Q., Ji, W.H., Dong, G.C., Sui, Q.L., Liu, Y.S., Yuan, H.L., Mo, X.X., 2012. Cambrian bimodal volcanism in the Lhasa Terrane, southern Tibet: record of an early Paleozoic Andean-type magmatic arc in the Australian proto-Tethyan margin. Chemical Geology 328, 290–308.

Zhu, D.C., Zhao, Z.D., Niu, Y.L., Dilek, Y., Hou, Z.Q., Mo, X.X., 2013. The origin and pre-Cenozoic evolution of the Tibetan Plateau. Gondwana Research 23, 1429–1454.

Zou, Y.Q., Huang, W.T., Liang, H.Y., Wu, J., Lin, S.P., Wang, X.Z., 2015. Identification of porphyry genetically associated with mineralization and its

zircon U-Pb and biotite Ar-Ar age of the Xiongcun Cu-Au deposit, Southern Gangdese, Tibet. Acta Petrologica Sinica 31, 2053–2062 (in Chinese with English abstract).

Figure captions:

Figure 1 (a) Tectonic framework of the Tibetan Plateau showing its major subdivisions (Zhu et al., 2013). (b) Schematic geological map of the central and eastern section of the Lhasa terrane modified from Pan et al. (2004), showing the study area, and the spatial and temporal distributions of the Late Triassic−Early Jurassic intrusive-volcano rocks in the central and southern Lhasa subterranes. (c) Geological map of the Basong Tso area. (d) Geological map of the Mamba area. Abbreviations: NLT = Northern Lhasa subterrane; CLT = Central Lhasa subterrane; SLT = Southern Lhasa subterrane; JSSZ = Jinsha Suture zone; BNSZ = Bangong-Nujiang Suture zone; IYZSZ = Indus-Yarlung Zangbo Suture zone; SNMZ = Shiquanhe-Nam Tso Mélange Zone; LMF = Luobadui-Mila Mountain Fault. Date sources: Zircon U-Pb ages in CLT (Luoza: 217−202 Ma, Chu et al., 2006; Zhang et al., 2007a; Ningzhong: 213−190 Ma, Kapp et al., 2005; Liu et al., 2006; Mamba: 210−195 Ma, He et al., 2006; Zhu et al., 2011; Sumdo: 201−190 Ma, Li et al., 2009; Yu et al., 2018; Jinda: 193−183 Ma, Zhu et al., 2011), Zircon U-Pb ages in SLT (Xiongcun: 195−172 Ma, Lang et al., 2014a, b; Qu et al., 2007; Tafti et al., 2009, 2014; Tang et al., 2010; Wang et al., 2017a; Xu et al., 2017a; Zou et al., 2015; Dongga: 192−172 Ma, Guo et al., 2013; Tan, 2012; Wang et al., 2017b; Xu et al., 2017b;

749 Namling: 212−207 Ma: Ma et al., 2017; Dazhuka: 205−170 Ma, Chu et al., 2006; Guo
750 et al., 2013; Ji et al., 2009; Meng et al., 2016b; Nyemo: 180−178 Ma, Guo et al., 2013;
751 Meng et al., 2016b; Zhang et al., 2007b; Quxu: 220−210 Ma, Ma et al., 2018; Meng et
752 al., 2016a; Qulong: 182 Ma, Yang et al., 2008; Sangri: 190−179 Ma, Dong and Zhang,
753 2013; Shui et al., 2018; Gyaca: 201−197 Ma, Dong and Zhang, 2013; Shui et al., 2018;
754 Xu et al., 2019; Zhongsa: 203−192 Ma, Zhu et al., 2011).
755
756 Figure 2 Field photos and photomicrographs of representative diorite and granodiorite
757 cumulates from the Basong Tso area. (a) The Early Jurassic (J_1) diorite cumulate
758 intruding the Late Triassic−Early Jurassic (T_3-J_1) metamorphic rocks. (b) The Early
759 Jurassic diorite cumulate intruding the granodiorite cumulate. (c) Outcrop of the Early
760 Jurassic diorite cumulate. (d) Outcrop of the Early Jurassic granodiorite cumulate. (e)
761 and (f) The mineral assemblage of diorite cumulate (under PPL). (g) The mineral
762 assemblage of granodiorite cumulate (under XPL). Amp, amphibole; Ap, apatite; Bt,
763 biotite; Ep, epidote; Pl, plagioclase; Qz, quartz; Ttn, titanite.
764
765 Figure 3 Field photos and photomicrographs of granitoids from the Mamba area. (a)
766 The Late Triassic−Early Jurassic granitoids intruding the Ordovician strata. (b)
767 Outcrop of the Mamba granitoids. (c) and (d) Outcrop showing the contact of MMEs
768 of varying size within their host granitoids. (e) The mineral assemblage of the host
769 granite (under XPL). (f) and (g) The mineral assemblage of the host granodiorite
770 (under PPL). (h) The sharp contact between MME and their host rocks, showing

771 MME being more fine-grained than the host rocks (under PPL). (i) The mineral
772 assemblage of quartz monzodiorte MME (under XPL). Amp, amphibole; Ap, apatite;
773 Bt, biotite; Ep, epidote; Kfs, K-feldspar; Pl, plagioclase; Qz, quartz; Ttn, titanite.
774
775 Figure 4 Representative compositions of plagioclase and amphibole from the Early
776 Jurassic intrusions in the central Lhasa subterrane. (a) Feldspar (anorthite (An)-albite
777 (Ab)-orthoclase (Or)) compositional diagram from Deer et al. (1992). (b)
778 Classification of amphiboles according to Leake et al. (1997).
779
780 Figure 5 Classification diagrams of the Early Jurassic intrusions in the central Lhasa
781 subterrane. (a) Classification of the plutonic rocks using CIPW norms (Le Bas and
782 Streckeisen, 1991). (b) AFM diagram after Wager and Deer (1939) with
783 discriminatory lines of Irvine and Baragar (1971) dividing the calc-alkaline and
784 tholeiitic magma series. (c) SiO_2 (wt.%) vs K_2O (wt.%) diagram (Peccerillo and
785 Taylor, 1976). (d) SiO_2 (wt.%) vs A/CNK diagram. Literature Data for the Late
786 Triassic-Early Jurassic Mamba host rocks are from He et al. (2005, 2006).
787
788 Figure 6 SiO_2 variation diagrams of TiO_2, Al_2O_3, TFeO, MgO, CaO and Na_2O (wt.%)
789 for the Early Jurassic intrusions in the central Lhasa subterrane. Bulk-rock: bulk-rock
790 major element compositions; av. Pl: average plagioclase major element compositions;
791 av. Amp: average amphibole major element compositions; Bulk-rock of start material:
792 bulk-rock major element compositions of experimental starting material; Melt:

793 experimentally determined major element compositions of equilibrium crystallization
794 melt.
795
796 Figure 7 Chondrite-normalized REE and primitive-mantle-normalized multi-element
797 patterns for the Early Jurassic intrusions in the central Lhasa subterrane. (a) and (b)
798 Diorite cumulate from the Basong Tso area. (c) and (d) Granodiorite cumulate from
799 the Basong Tso area. (e) and (f) Host granitoids and MME from the Mamba area.
800 Literature data for the Late Triassic-Early Jurassic Mamba host rocks are from He et
801 al. (2005, 2006); Average ocean crust composition are from Niu and O'Hara (2003);
802 Data of upper, middle and lower crust are from Rudnick and Gao (2003).
803
804 Figure 8 Bulk-rock SiO_2 (wt.%) vs $\varepsilon_{Nd}(t)$ for the Early Jurassic diorite and
805 granodiorite cumulates from the Basong Tso area in the central Lhasa subterrane. The
806 data of the Sumdo eclogite are from Li ZL et al. (2009) and Zeng et al. (2009). Binary
807 mixing calculations are between N-MORB (average composition: $\varepsilon_{Nd}(t)$ = 10.04, SiO_2
808 = 50.46 wt.%, Nd = 11.32 ppm are from Niu et al. (2002b)) and lower crust (average
809 composition of $\varepsilon_{Nd}(t)$ = -18.52 is from Ben et al. (1984), SiO_2 = 53.4 wt.% and Nd =
810 11 ppm are from Rudnick and Gao (2003)), and upper crust (average composition:
811 $\varepsilon_{Nd}(t)$ = -12.40 is from Harris et al. (1988b), SiO_2 = 66.6 wt.% and Nd = 27 ppm are
812 from Rudnick and Gao (2003)). The mixing lines are calculated after Faure (1977)
813 with 10 % intervals shown.
814

Figure 9 Cathodoluminescence images of the representative zircons of the Early Jurassic intrusions in the central Lhasa subterrane. The circles are the analytical spots with ages in Ma.

Figure 10 Zircon U-Pb concordia diagrams for the Early Jurassic intrusions in the central Lhasa subterrane.

Figure 11 Zircon U-Pb ages vs $\varepsilon_{Hf}(t)$ diagram for the Late Triassic–Early Jurassic intrusions from the central and southern Lhasa subterranes.

Data sources: Plutonic rocks ($SiO_2 \geq 55\%$) in the CLT are from Zhang et al. (2007a), Zhu et al. (2011) and Yu et al. (2018); Plutonic rocks ($SiO_2 \geq 55$ %) in the SLT are from Chu et al. (2006), Dong and Zhang (2013), Guo et al. (2013), Ji et al. (2009), Meng et al. (2016b), Shui et al. (2016, 2018), Xu et al. (2019), Yang et al. (2011), Zhang et al. (2007b), Zhu et al. (2011),; Plutonic rocks (55 % > SiO_2 > 45 %) in SLT are from Meng et al. (2016a), Shui et al. (2018), Xu et al. (2019).

Figure 12 SiO_2 (wt.%) variation diagrams of Dy/Yb, Eu (ppm) and La/Sm for the Early Jurassic intrusions from the Mamba area in the central Lhasa subterrane. Literature data for the Late Triassic−Early Jurassic Mamba host rocks are from He et al. (2005, 2006).

Figure 13 The range and spatial distribution of zircon $\varepsilon_{Hf}(t)$ from the Late

837 Triassic−Early Jurassic (~215−170 Ma) intrusions in the central and southern Lhasa
838 subterranes. (a) Zircon $\varepsilon_{Hf}(t)$ plotted against sample latitude of 29.1°−30.2°N at the
839 longitude of 88.6-93.9°E. (b) Zircon $\varepsilon_{Hf}(t)$ plotted against sample latitude of
840 29.1°−30.2°N at longitude of 88.6−90.6°E. (c) Zircon $\varepsilon_{Hf}(t)$ plotted against sample
841 latitude of 29.1°−30.2°N at longitude of 91.6−93.9°E. Data sources are the same as in
842 Figure 11.
843
844 Figure 14 Cartoons showing the Late Triassic−Early Jurassic magmatism and crustal
845 evolution in the central and southern Lhasa subterranes. (a) During 215−196 Ma,
846 magmas in the SLT are derived from mantle with minor ancient crustal assimilation at
847 the northernmost; magmas in the CLT are derived from hydrated ocean crust together
848 with much subducted sediments. (b) During 195−175 Ma, magmas in the SLT are
849 derived from mantle with much less ancient crustal assimilation; magmas in the CLT
850 are derived from much more hydrated ocean crust together with ancient crust. Zircon
851 $\varepsilon_{Hf}(t)$ data sources are the same as in Figure 11. Black dashed line shows the
852 subterrane bounding between the SLT and the CLT, i.e., Luobadui-Mila Mountain
853 Fault zone in Figure 1b. Abbreviations: SCLM = subcontinental lithospheric mantle;
854 MASH = melting-assimilation-storage-homogenization zone.

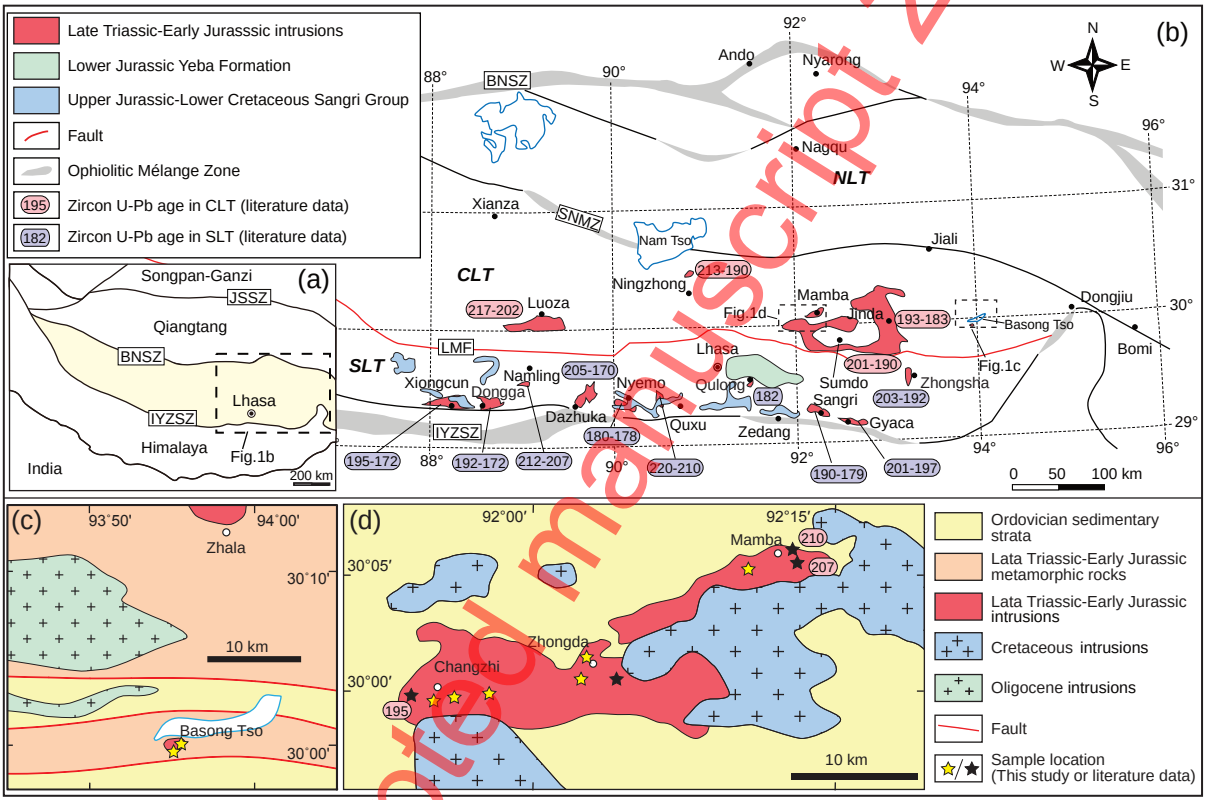

Figure 1

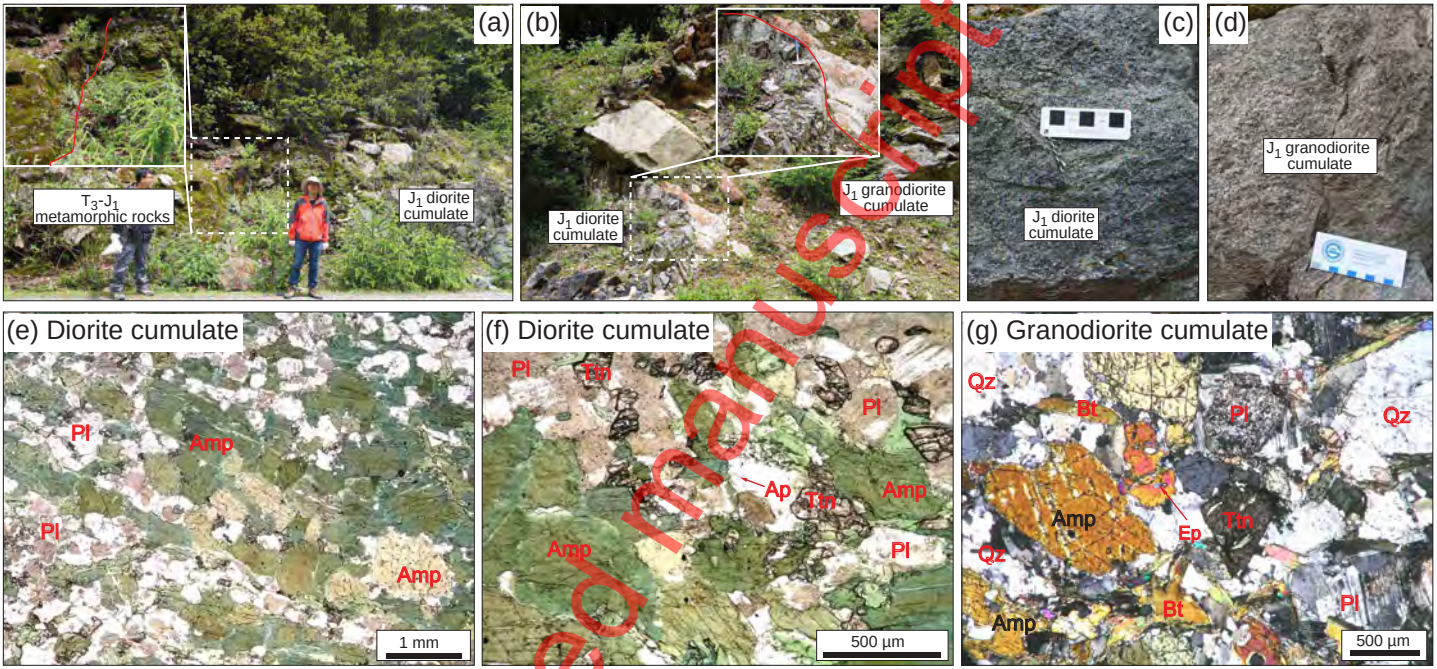

Figure 2

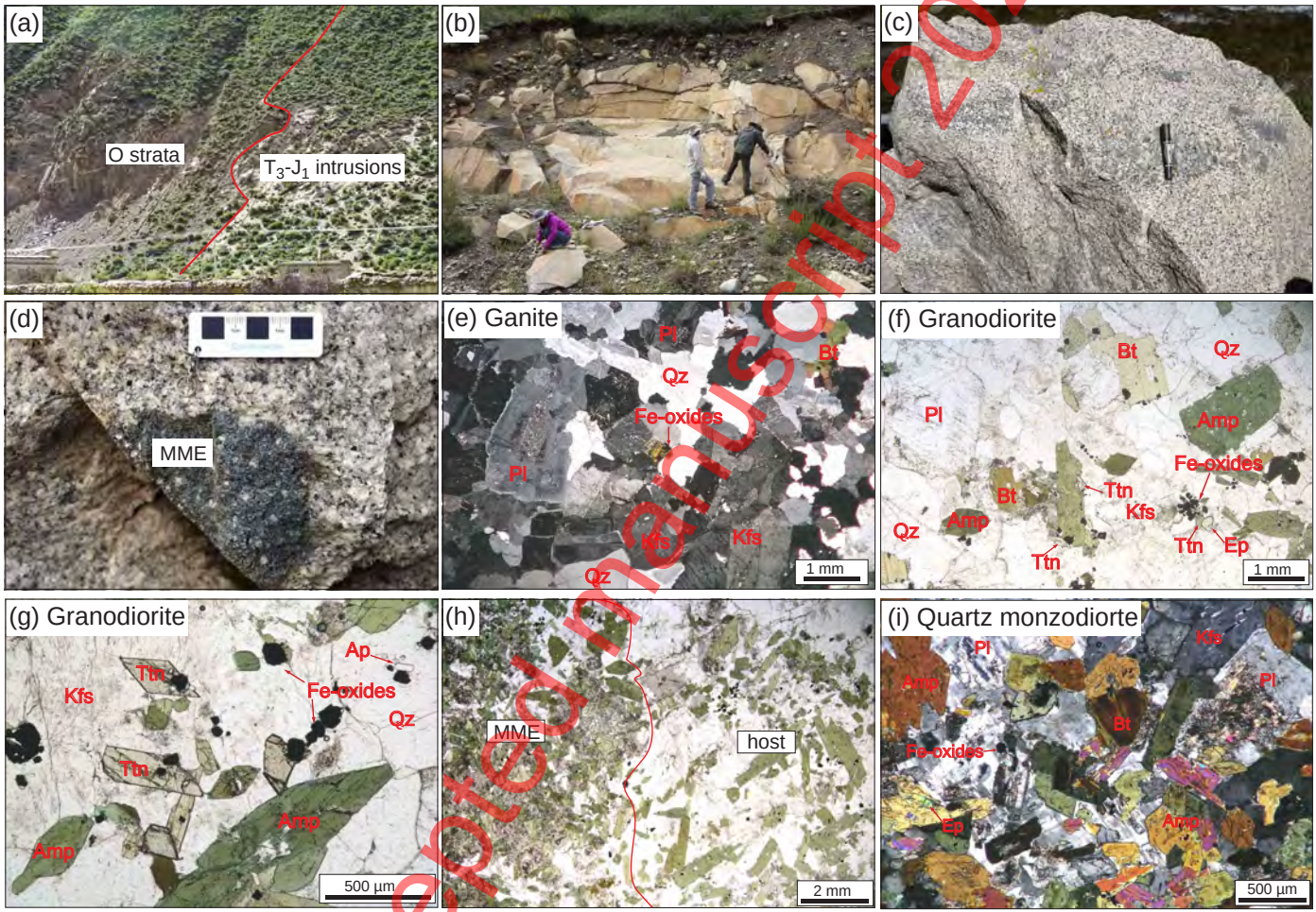

Figure 3

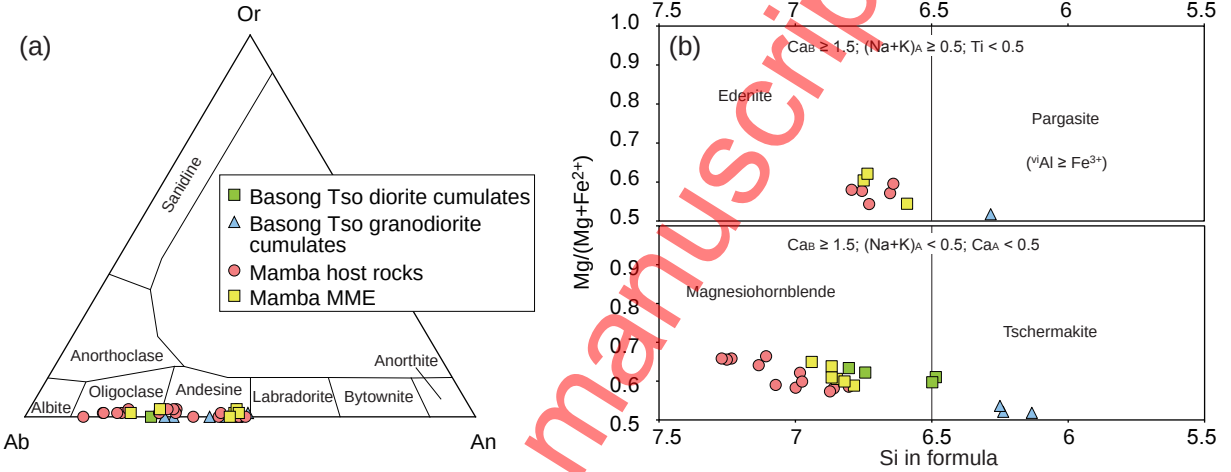

Figure 4

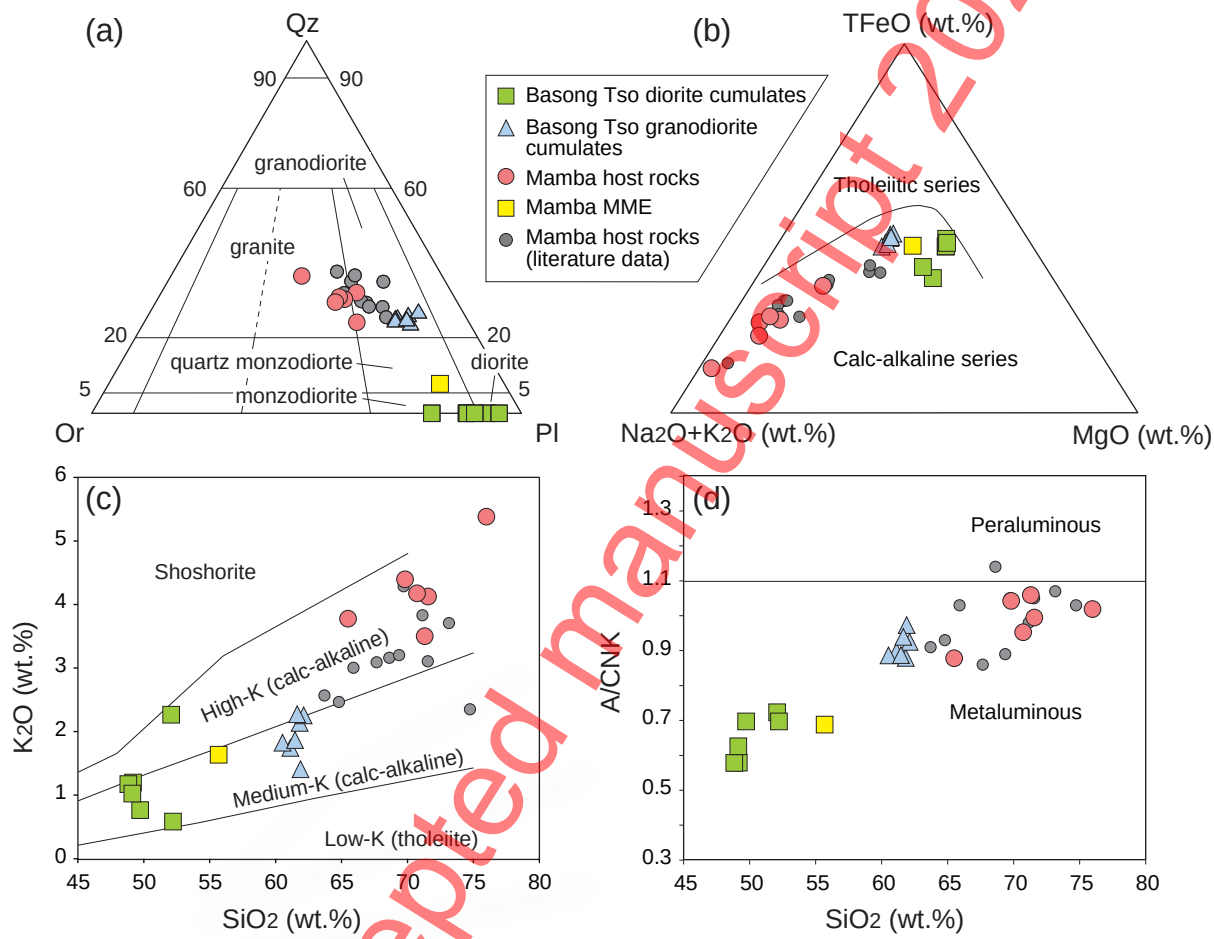

Figure 5

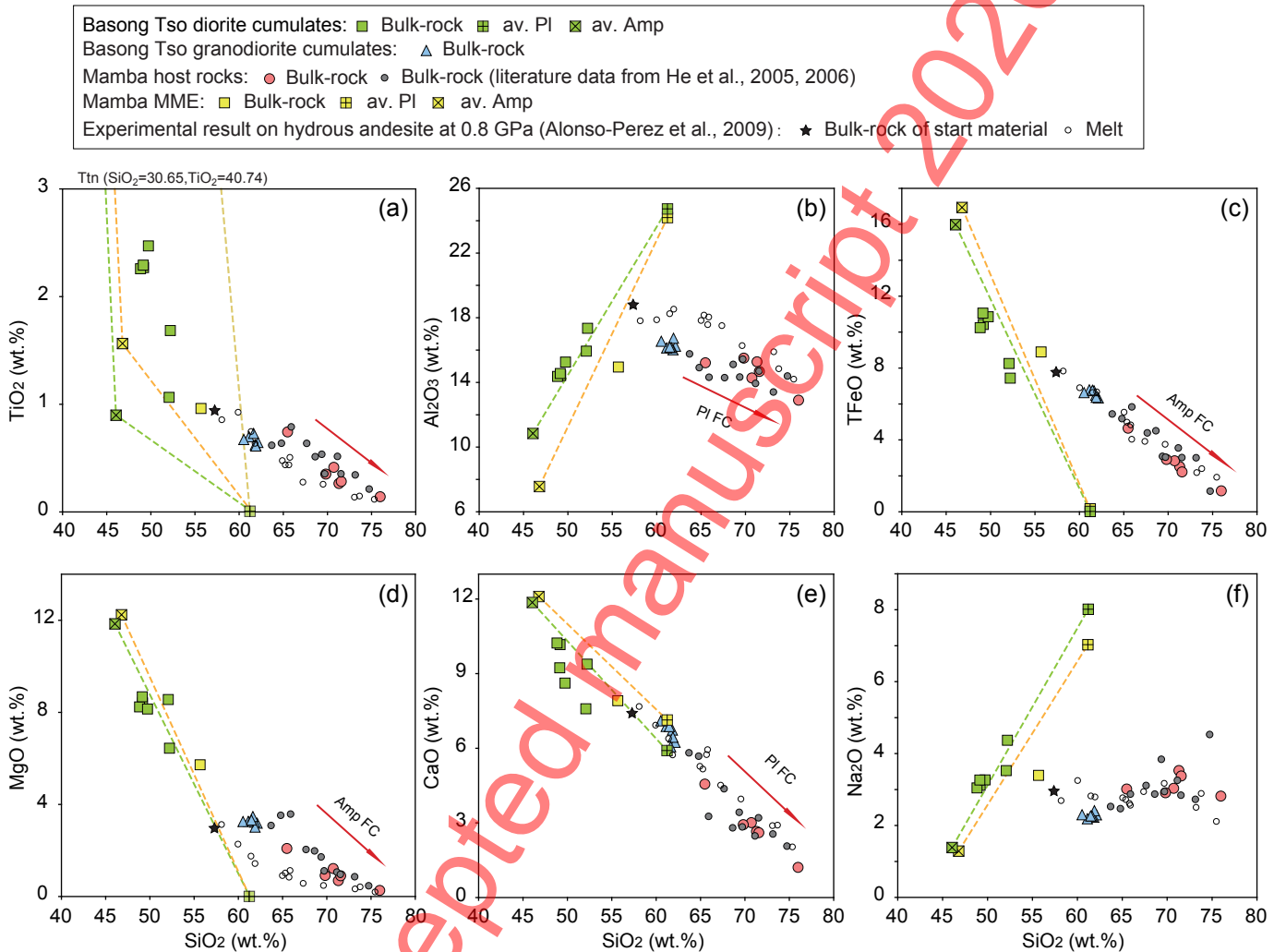

Figure 6

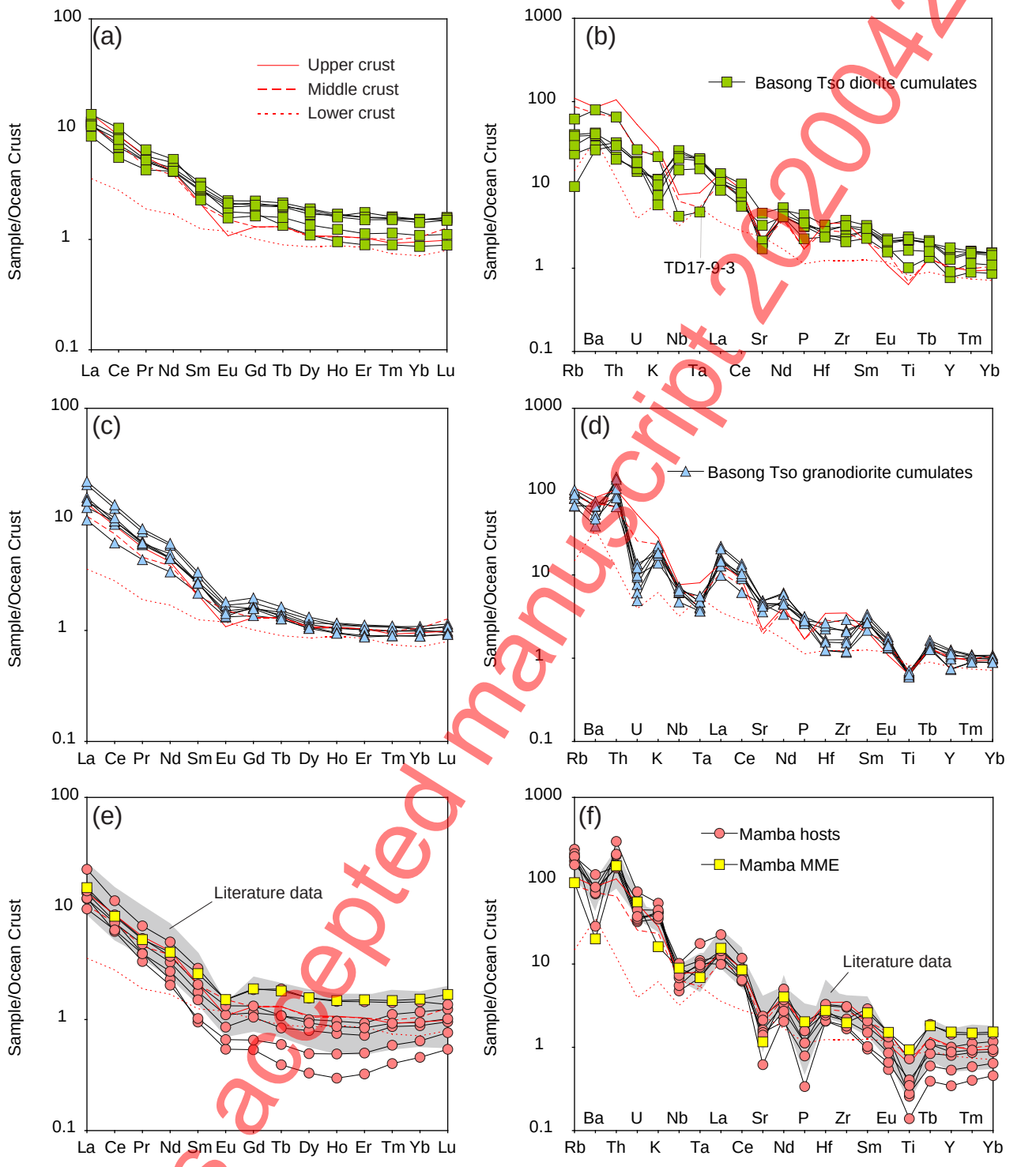

Figure 7

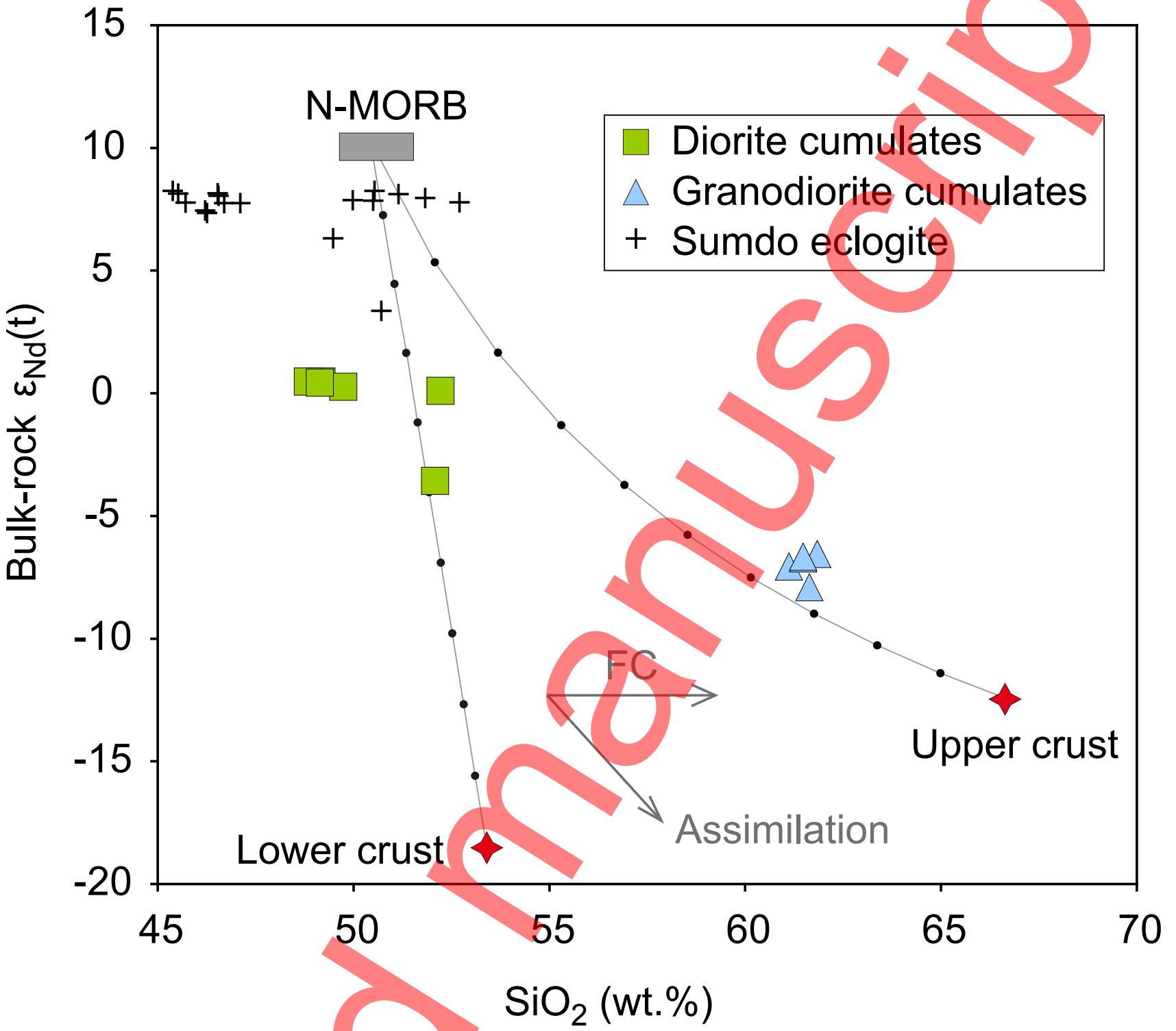

Figure 8

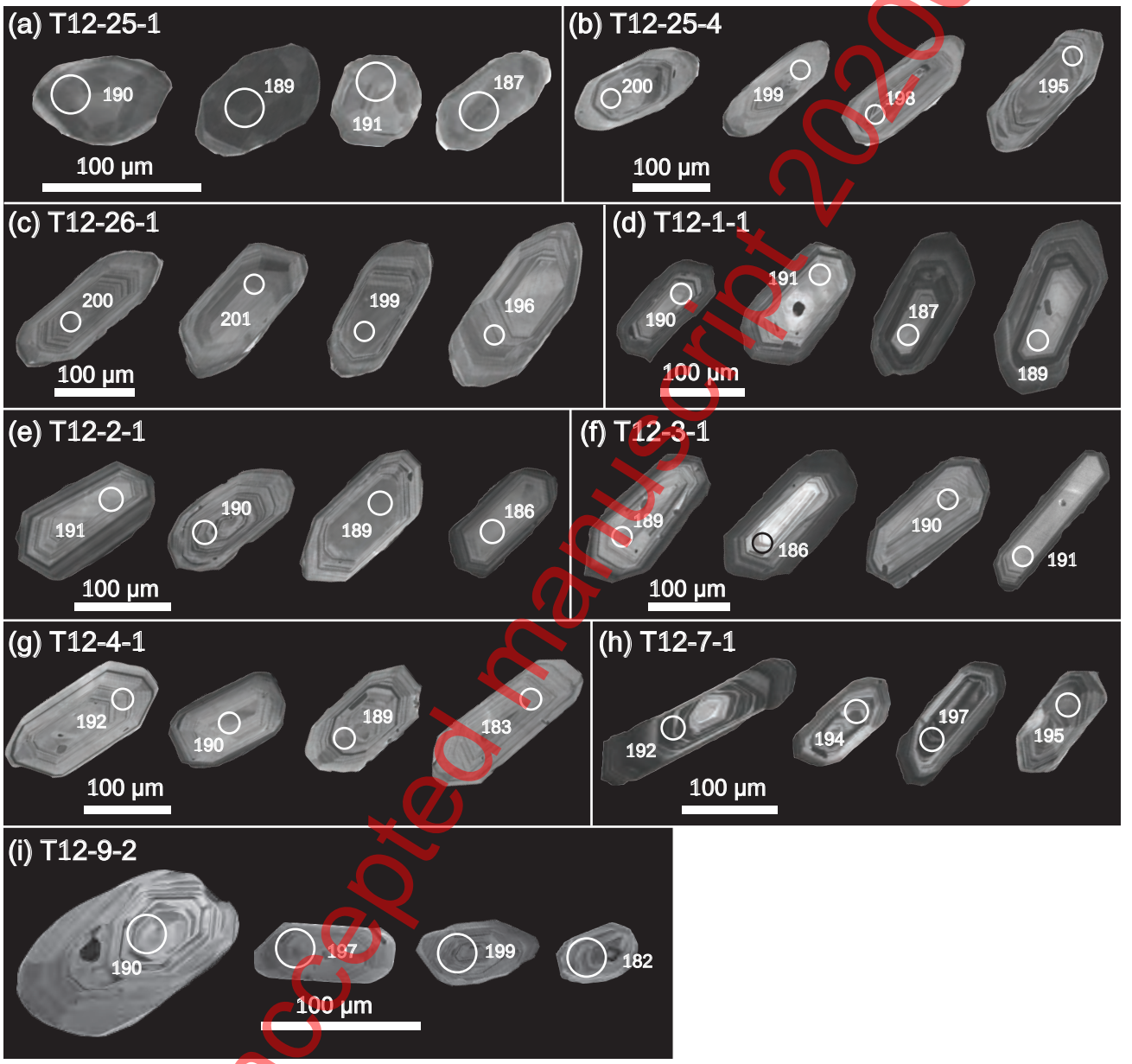

Figure 9

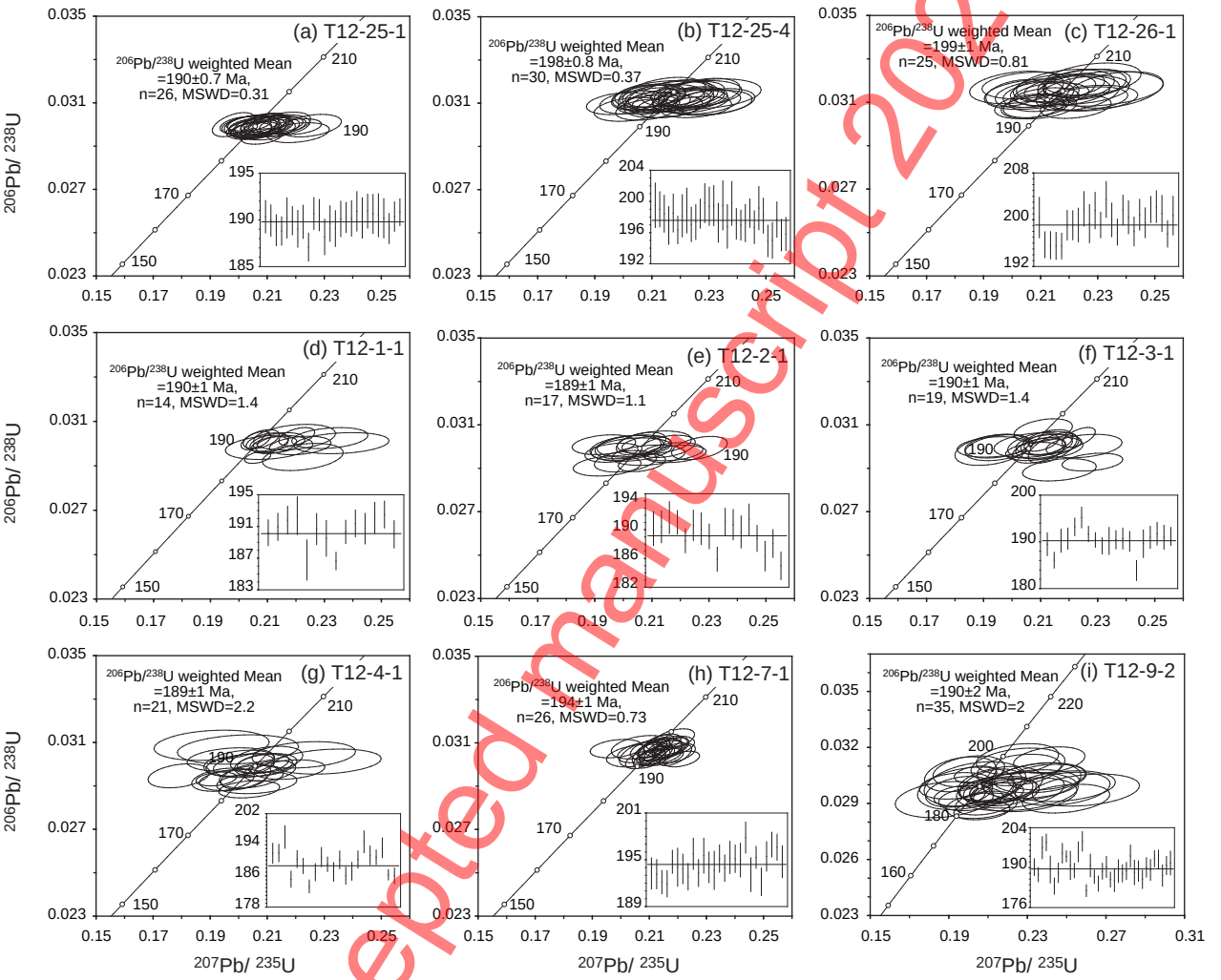

Figure 10

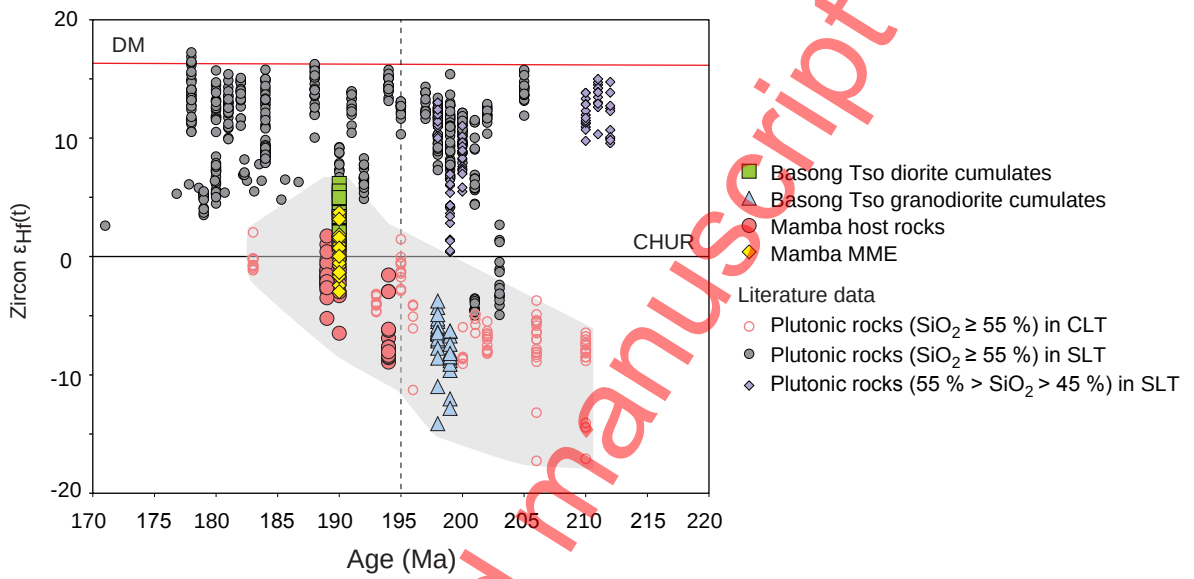

Figure 11

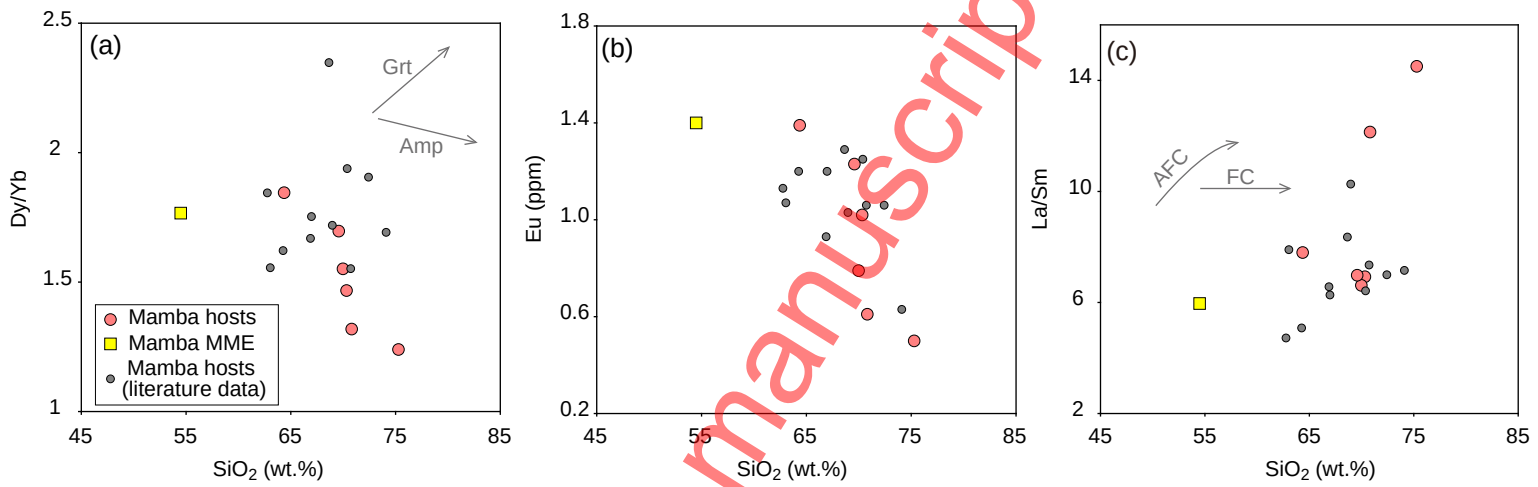

Figure 12

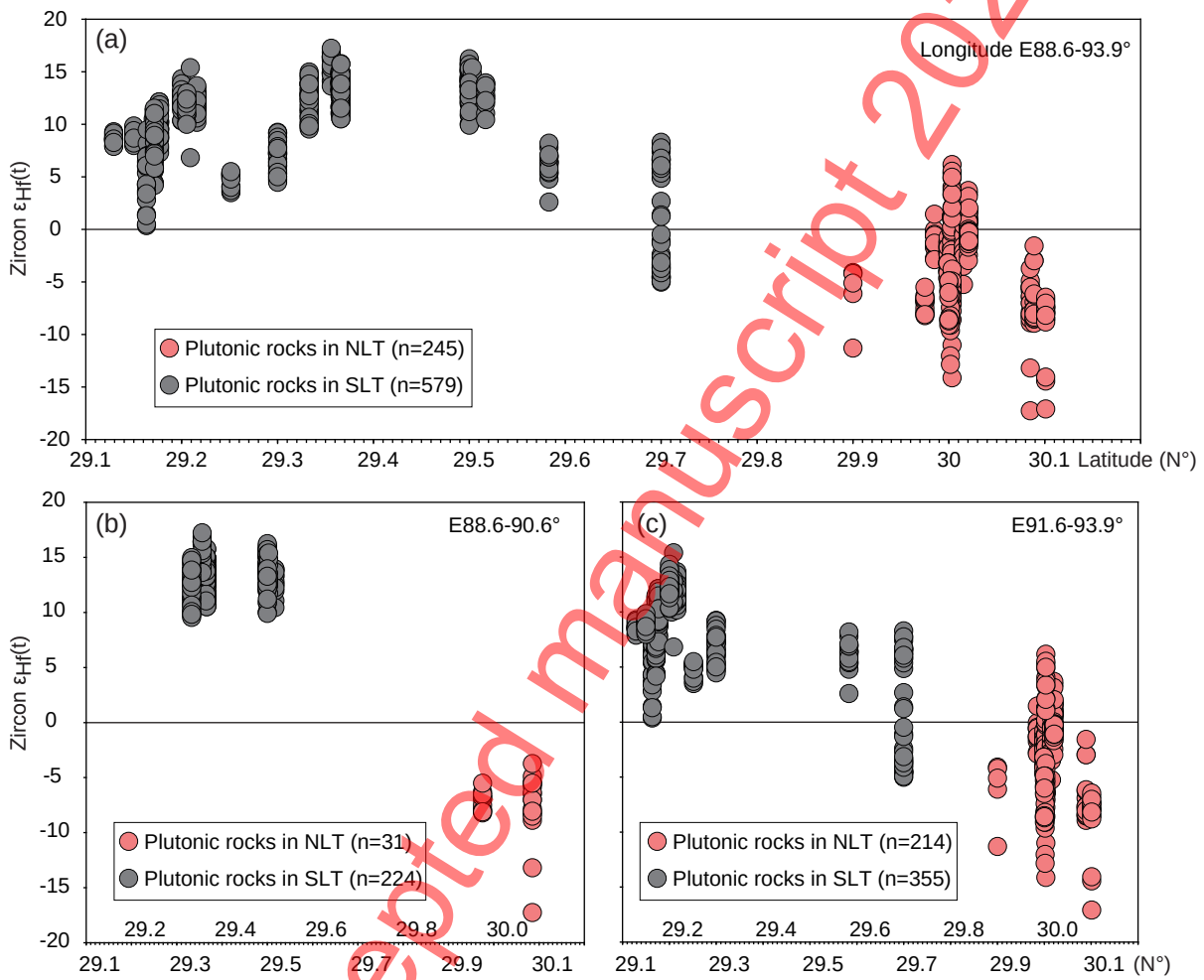

Figure 13

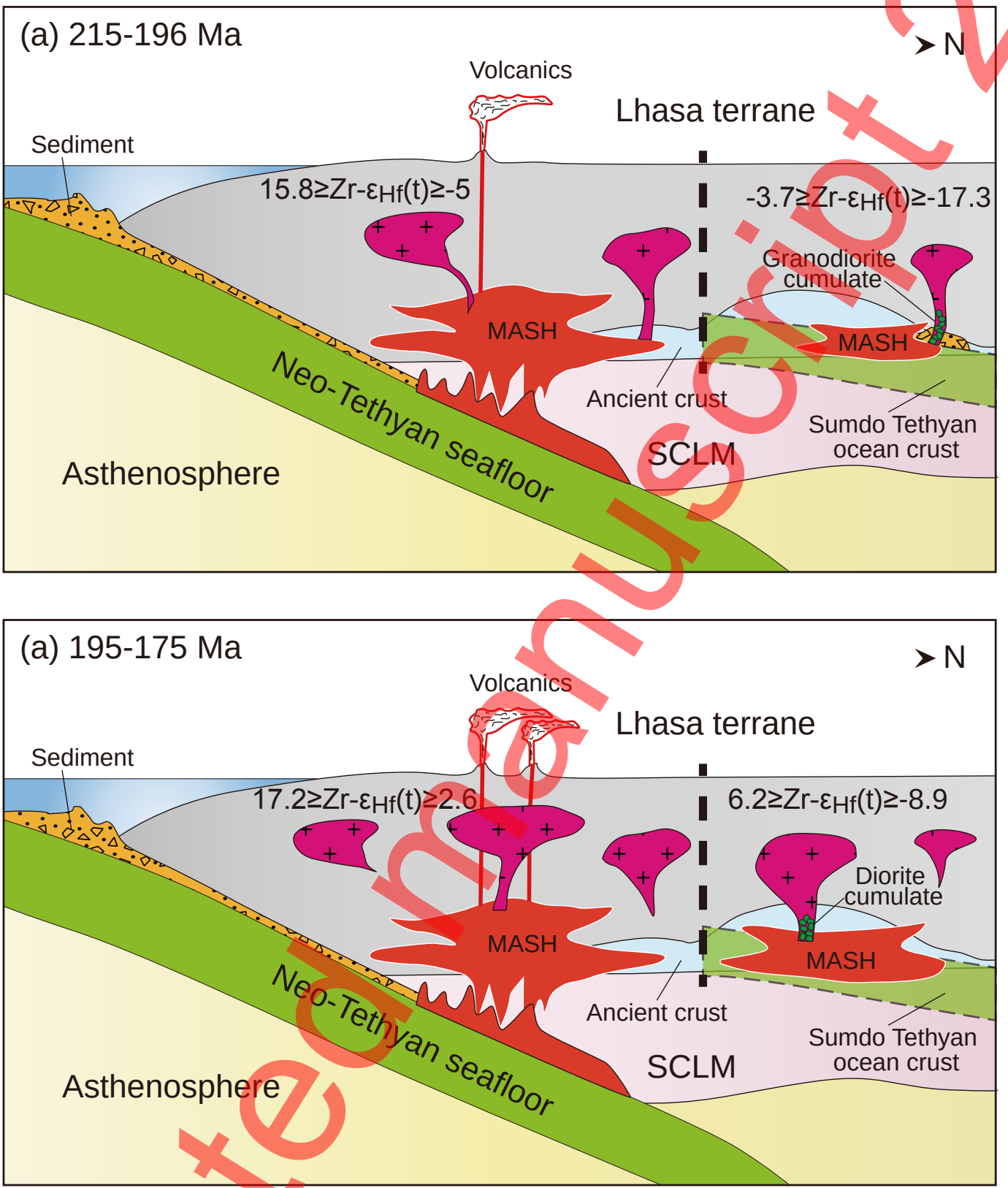

Figure 14